TURUN YLIOPISTO
Matemaattis-luonnontieteellinen tiedekunta

Seasonal Cycle of Sedimentation and Sediment characteristics in Subarctic Lake Kevojärvi

Sofia Muurinen

Geology (Quaternary Geology)
Master’s thesis
Credits: 30 ECTS

15.6.2026
Turku

Master's thesis

Subject: Quaternary Geology
Author: Sofia Muurinen
Title: Seasonal Cycle of Sedimentation and Sediment characteristics in Subarctic Lake Kevojärvi
Supervisor: Saija Saarni
Number of pages: 59 pages + 7 appendices
Date: 15.6.2026

Northern Hemisphere high-latitude lakes are in the forefront of the global climate warming, subjected to the rapid changes in their water column and catchment. In favourable conditions, traces of these responses to climate forcing are preserved in lake sediments. However, the hydroclimatic signals in sedimentary archives cannot be utilized without further understanding of the depositional processes in the lake. In this study, near-bottom sediment trapping alongside hydrological monitoring was carried out between 2019 and 2023 to investigate seasonal sedimentation and the related sediment characteristics in subarctic Lake Kevojärvi, Finland. Sediment sampling was conducted in two depositional environments, basin and delta. Sediment geochemistry was determined by micro-X-ray fluorescence (μ-XRF) spectrometry. Seasonal sedimentation was controlled by detrital input associated with changes in transport energy. At the annual scale, sediment accumulation was dominated by the snowmelt-induced spring floods. In contrast, sedimentation was negligible under the winter ice cover. As a result, sample sufficiency was the main limiting factor in this study. According to the principal component analysis (PCA), spring sediments were representative of the lithogenic fraction, whereas summer and winter were accompanied by the redox-sensitive elements. Therefore, redox-related post-depositional processes were expected to contribute to the seasonal variability in sediment characteristics. Nevertheless, Mn/Fe ratio was not suitable for detecting changes in redox conditions in this lake. Overturn occurred twice a year oxygenating the bottom waters, while persistent stratification was followed by hypolimnetic anoxia in winter and summer. However, cool air temperatures weakened summer stratification, and when preceded by intense spring flood in summer 2020, water column remained unstratified. This may indicate a change from occasionally monomictic to strongly dimictic mixing regime in the warming future summers. Overall, the findings showed that the sedimentation and sediment characteristics reflected the seasonal changes occurring in the Lake Kevojärvi and its catchment. These enhance understanding of paleoenvironmental signals preserved in the lake's annually laminated sediments. Monitoring is still ongoing in the Lake Kevojärvi basin, allowing documentation of responses to climate forcing in the future. Further analyses of grain size and organic matter are suggested.

Key words: Geochemistry, Lake sediments, Micro-XRF, Seasonality, Sediment trap

Pro gradu -tutkielma

Pääaine: Maaperägeologia
Tekijä: Sofia Muurinen
Otsikko: Seasonal Cycle of Sedimentation and Sediment characteristics in Subarctic Lake Kevojärvi
Ohjaaja: Saija Saarni
Sivumäärä: 59 sivua + liitteet 7 sivua
Päivämäärä: 15.6.2026

Korkeiden leveysasteiden järvet pohjoisella pallonpuoliskolla ovat ilmaston globaalin lämpenemisen keskiössä, jossa niiden vesipatsaat ja valuma-alueet altistuvat nopeille muutoksille. Suotuisissa olosuhteissa vaste näihin ilmastollisiin muutoksiin tallentuu järvisedimentteihin. Sedimentteihin tallentuneita ilmastollisia signaaleja ei voida kuitenkaan hyödyntää tuntematta järven kerrostumisprosesseja. Tässä tutkimuksessa pohjasedimenttikeräimiä ja hydrologista monitorointia käytettiin subarktisen Kevojärven sedimenttien kerrostumisen ja koostumuksen vuodenaikaisvaihtelun havainnointiin vuosina 2019–2023. Sedimenttinäytteet kerättiin kahdesta kerrostumisympäristöstä, syvänteestä (basin) ja jokisuusta (delta). Sedimenttien geokemia määritettiin mikroröntgenfluoresenssispektrometrialla (μ-XRF). Kuljetusenergian muutoksiin kytkeytyvä järveen kulkeutuva rapautumisperäinen aines hallitsi sedimentaation vuodenaikaisvaihtelua. Vuositasolla sedimenttien kerrostumista dominoivat lumensulamisen aikaansaamat kevättulvat. Talvisin jääpeitteenalainen sedimentaatio oli lähes olematonta, minkä vuoksi näytteiden riittävyys oli tutkimuksen suurin rajoittava tekijä. Pääkomponenttianalyysin (PCA) perusteella kevätsedimentaatiossa korostuivat kiviainesperäiset alkuaineet, kun taas kesä ja talvi edustivat hapetus-pelkistysreaktioille herkkiä alkuaineita. Näin ollen hapettumiseen ja pelkistymiseen (redox) liittyvien kerrostumisen jälkeisten prosessien odotettiin vaikuttavan sedimenttien vuodenajoista riippuvaan koostumukseen. Mn/Fe suhde ei kuitenkaan sopinut redox-olosuhteiden muutosten havaitsemiseen tässä järvessä. Alusveden hapettava täyskierto tapahtui kahdesti vuodessa, kun taas hapettomat olosuhteet olivat seurausta pitkäkestoisesta kerrostuneisuudesta talvisin ja kesäisin. Matalat kesälämpötilat kuitenkin heikensivät lämpötilakerrostuneisuutta ja kun kesällä 2020 tällaisia olosuhteita edelsi intensiivinen kevättulva sitä ei muodostunut. Kesien lämmetessä tämä voi merkitä muutosta ajoittain monomiktisestä vahvasti dimiktiseen kerrostumiskiertoon. Kaiken kaikkiaan tulokset osoittivat, että sedimenttien kerrostuminen ja koostumus heijastelivat Kevojärvessä ja sen valuma-alueella tapahtuvia vuodenaikaisvaihteluita. Nämä tarkentavat järven vuosikerroksellisiin sedimentteihin tallentuneiden paleoympäristöä kuvaavien signaalien tulkintaa. Seurannan jatkuminen Kevojärven syvänteessä mahdollistaa järven ilmastollisen vasteen taltioinnin myös tulevaisuudessa. Raekoon ja orgaanisen aineksen tarkempia määrityksiä suositellaan.

Avainsanat: geokemia, järvisedimentit, mikro-XRF, sedimenttikeräin, vuodenaikaisvaihtelu

Contents

1 Introduction

Northern Hemisphere is under an irreversible change regarding the climate warming and other, known and yet-to-be understood, impacts of climate change. The farther north, the more rapid the change, as the accelerating warming of the Arctic was estimated to be even four times faster than the global mean trend over 1979–2021 (Rantanen *et al.*, 2022). Concurrently, majority of the world's lakes lie in Northern hemisphere, within the formerly glaciated area of the Late Glacial Maximum, present-day boreal and subarctic regions (Messager *et al.*, 2016).

Subarctic Lake Kevojärvi in northernmost Finland is in the hot spot, subject to these changes reflected in the lacustrine environment, such as increasing water temperature, switching mixing regime, and decreasing oxygen levels (Jane *et al.*, 2023; Jansen *et al.*, 2024; Lincoln *et al.*, 2025). Not only do lakes undergo changes, but also record them in the sediments, specifically at the deep basin (Ojala *et al.*, 2013). Physical and chemical composition of the sediments provide insight into the prevailing environmental conditions in the lake as well as in its catchment.

Sediment characteristics are preserved in annually laminated sediments, also present in Lake Kevojärvi (Haltia *et al.*, 2021), from which paleoenvironments can be reconstructed. However, accurate reconstructions, whether past or future, require knowledge of modern sedimentation, which can be achieved by sediment trapping (Ojala *et al.*, 2013; Saarni *et al.*, 2023). Lake Kevojärvi provides ideal conditions to study modern sedimentation in a pristine, yet accessible, subarctic area due to the Kevo Research Station located by the lake.

In this study, near-bottom sediment-trap sampling was conducted at the delta and the basin in Lake Kevojärvi over four years, concurrently with the hydrological monitoring. The aim was to investigate intra- and interannual variations of seasonal sedimentation and sediment characteristics in relation to the actual depositional conditions. The observations of these interactions were enhanced with micro-X-ray fluorescence analysis of sediment geochemistry. Overall, the focus was on understanding the current seasonal sedimentation and hydrological conditions, and their future responses to the rapid environmental change occurring in subarctic Lake Kevojärvi and its catchment.

2 Background

2.1 Lacustrine environments in relation to changing climate

The most direct global response to climate change in present-day lacustrine environments is the warming surface waters, as shown in numerous studies (e.g., Schmid *et al.*, 2014; O'Reilly *et al.*, 2015; and reviewed in Woolway *et al.*, 2020). Over the last few decades, this has led to strengthened and prolonged periods of thermal stratification in northern hemisphere lakes (Mammarella *et al.*, 2018) inhibiting lake mixing, and hence resulting in longer periods of oxygen depletion in hypolimnion even in oligotrophic lakes (Jane *et al.*, 2023; Jansen *et al.*, 2024). In addition, longer open water periods (Benson *et al.*, 2012; Sharma *et al.*, 2019; Li *et al.*, 2022) have enabled earlier onset of thermal stratification and warmer surface water temperatures in summer. Covering the last six decades, increased surface water temperatures, strengthened stratification, shorter ice-cover period, and decrease in snow depth were observed by Noori *et al.* (2022) for Lake Inarijärvi, the largest lake in Finnish Lapland located less than 100 km southeast of Lake Kevojärvi. They also detected a decrease in water transparency, although browning, driven by increased dissolved organic matter and Fe associated with it, is more typical of boreal lakes under stronger anthropogenic interference (Xiao & Riise, 2021).

Climate warming is shifting seasons and their duration regarding seasonal temperatures (Woolway, 2023). The described processes occurring in lake and its catchment are tied to seasonal variability. These processes and prevailing seasonal conditions are in control of transport, deposition, and preservation of sediments, and hence seasons alter the cycle of sedimentation and the composition of deposited sediments in lakes (Håkanson & Jansson, 2002). In high latitudes, the present-day sedimentation is dominated by spring floods associated with snowmelt-induced discharge and pronounced catchment erosion reflecting the prevailing conditions of the preceding winter (Snowball *et al*., 1999; Ojala *et al.*, 2013; Saarni *et al.*, 2017). In summer, the autochthonous proportions of organic matter in sediments increases due to the primary production in lake (Snowball *et al*., 1999). Summer and autumn sedimentation is characterized by the open water conditions during which sedimentation is more subject to weather variability, including extreme events such as intense rainfall (Zillén *et al.*, 2003; Ojala *et al.*, 2013). In contrast, calm conditions during a long ice-cover period in winter allow the deposition of fine-grained organic matter (Ojala *et al.*, 2013; Saarni *et al.*, 2017).

Present-day observations are in accordance with the sedimentation and sediment characteristics associated with the most recent pre-industrial warm intervals, of which Medieval Climate Anomaly (MCA; ~950–1250 CE; Mann *et al.*, 2009) is temporally the most recent, whereas Holocene Thermal Maximum (HTM; generally ~11–5 ka BP, as summarized in Renssen *et al.*, 2009) provides the most recent analogue for the rapidly warming conditions in higher latitudes (Renssen *et al.*, 2012). There are no direct measurements, or globally standardized meteorological observations of the pre-industrial climate variations (IPCC, 2021). Therefore, past climates and environmental conditions are studied through proxies reflecting now measurable variables, such as air temperature and precipitation, in seasonal or annual resolution. In lakes, continuously deposited sediments act as archives where proxies are preserved through sedimentation processes (Birks & Birks, 2006). Physical, chemical, and biological materials (i.e., proxies) are either transported to or formed in the lake (Birks & Birks, 2006). Once settled, material in the sediment-water interface is still in interaction with the overlying water column, and therefore prone to the changes in the bottom-water conditions. For example, sediment geochemistry can be altered by the dissolution and precipitation of redox-sensitive elements indicating oxygen availability before burial (Jansen *et al.*, 2024; Lincoln *et al.*, 2025). In addition to the paleoclimatic reconstructions, proxies together with the present-day measurements and the analyses of the modern lake sediments and sedimentations are used in future projections (IPCC, 2021)

Organic proportion of the deposited sediments was shown to increase, while minerogenic matter decreased in boreal lakes during MCA (Tiljander *et al.*, 2003) and HTM (Lincoln *et al.*, 2025). The decreased minerogenic input to the lakes indicates weakened spring floods due to decreased, or non-existent, snow cover (Tiljander *et al.*, 2003; Lincoln *et al.*, 2025). Lincoln *et al.* (2025) suggest that thermal stratification was strengthened due to the warm summer temperatures of HTM, mobilizing redox-sensitive elements (Fe and Mn) into the hypolimnion under prolonged hypoxic and anoxic conditions. These further reinforced thermal stratification by the chemically denser hypolimnion and weaker transparency. However, they also reported Fe-rich sediment layers indicating events of oxygenation associated with climatic variability during HTM, resulting in episodic meromictic and dimictic mixing regimes. By comparison, fluctuations in lake mixing regime were not identified in any cold intervals (Lincoln *et al.*, 2025), of which Little Ice Age (LIA; ~1250–1860 CE; Wanner *et al.*, 2022) was the most recent. In general, colder climate results in predominantly minerogenic and less organic sedimentation (Zolitschka *et al.*, 2015), indicating increased catchment erosion and inhibited organic production (Ojala & Alenius, 2005; Meyer-Jacob *et al.*, 2017). In contrast to the pre-industrial Holocene climate variations, an immediate response to the modern climate change was detected by Meyer-Jacob *et al.* (2017) in the sediment record of a subarctic lake in Swedish Lapland.

With the globally warming air temperatures (IPCC, 2021; 2022), lake surface waters are expected to warm by 70–85 % of the projected air temperature increase at thermal equilibrium (Schmid *et al.*, 2014). Furthermore, the decrease in lake ice-cover period and its extent in Northern Hemisphere continues in an accelerating pace (IPCC, 2022), with even a month shorter ice-cover periods in the Arctic lakes by 2050 (IPCC, 2021). This, along with decreased snow cover, may advance the onset of spring floods and reduce their intensity (IPCC, 2021), thereby potentially lowering peak sediment accumulation in spring. In contrast, the projected increase in precipitation and runoff combined with an intensification of rain-on-snow (IPCC, 2021) and extreme snowfall events (Quante *et al.*, 2021) during winter in higher latitudes may in turn contribute to flooding. Prolonging open-water period and increasing temperatures will maintain the trend of the strengthening summer stratification in lakes, which in temperate areas is projected to result in the change of the mixing regime by the end of this decade (IPCC, 2022). For example, dimictic lakes are expected to become monomictic without a winter ice-cover (Woolway & Merchant, 2019). However, more research is needed, also underlined by IPCC (2022), particularly on lake-specific responses. Lake Kevojärvi is a case in point, as it is expected to retain a seasonal ice cover, e.g., What is the present-day and the projected mixing regime of this subarctic lake? This thesis project aims to contribute to regional coverage, with a particular focus on understanding the seasonality in Lake Kevojärvi and its unique responses to climate forcing.

2.2 Study area

Lake Kevojärvi (69º45′34"N, 27º00′23"E; 74.7 m a.s.l) is one of the mainly south-north oriented steep-sided fluvial lakes of Utsjoki River (Figure 1). It is located approximately 360 km north from the Arctic circle and lies less than 20 km south from the Finnish-Norwegian border where Tenojoki River, the mainstem of Utsjoki River, separates the two countries and then runs through Finnmark in Norway into the Barents Sea. Tsarsjoki and Kevojoki rivers combine to form a delta on the western side of the Lake Kevojärvi. Inflow and sedimentation in the western basin of the Lake Kevojärvi are controlled by these rivers (Haltia *et al.*, 2021). According to Haltia *et al.* (2021), annually laminated sediments (i.e., varves) are only present in this flat-bottomed western basin where the lake is at its deepest (35 m). Utsjoki, Tsarsjoki and Kevojoki rivers are the primary contributors to the oligotrophic Lake Kevojärvi's discharge, with some inflow from smaller streams (Haltia *et al.*, 2021). Lake Kevojärvi has a surface area of 1.02 km^2 and an outlet to Lake Jomppalanjärvi in the North (Syke, 2024). With a rather large catchment area (1520 km^2), these factors result in severe mean annual (247 cm) and maximum (447 cm) water level changes during spring floods that are typical of the lake (Syke, 2024).

The Kevo Research Station of the University of Turku is located on the land area that separates the western basin and the elongated part of Lake Kevojärvi (Figure 1). Finnish Meteorological Institute has collected weather data from the area since 1962 (University of Turku, 2026). The climate is subarctic, although relatively mild due to the maritime effect of the North Atlantic and Arctic Oceans (Haltia *et al.*, 2021). However, some of the Finland's highest and lowest temperatures have been measured at the Kevojärvi weather station (FMI, 2024c). Nevertheless, long cold winters and short cool summers are still characteristic of this climate area (Haltia *et al.*, 2021). During the 1991-2020 reference period, the annual mean temperature was -1.1 ºC and the mean precipitation was 484 mm (FMI, 2024d). Snow cover in the area lasts from October to May (Haltia *et al.*, 2021). The ice cover duration of the Lake Kevojärvi is approximately seven months, with ice freeze-up in October-November and ice breakup in May-June (Syke, 2024).

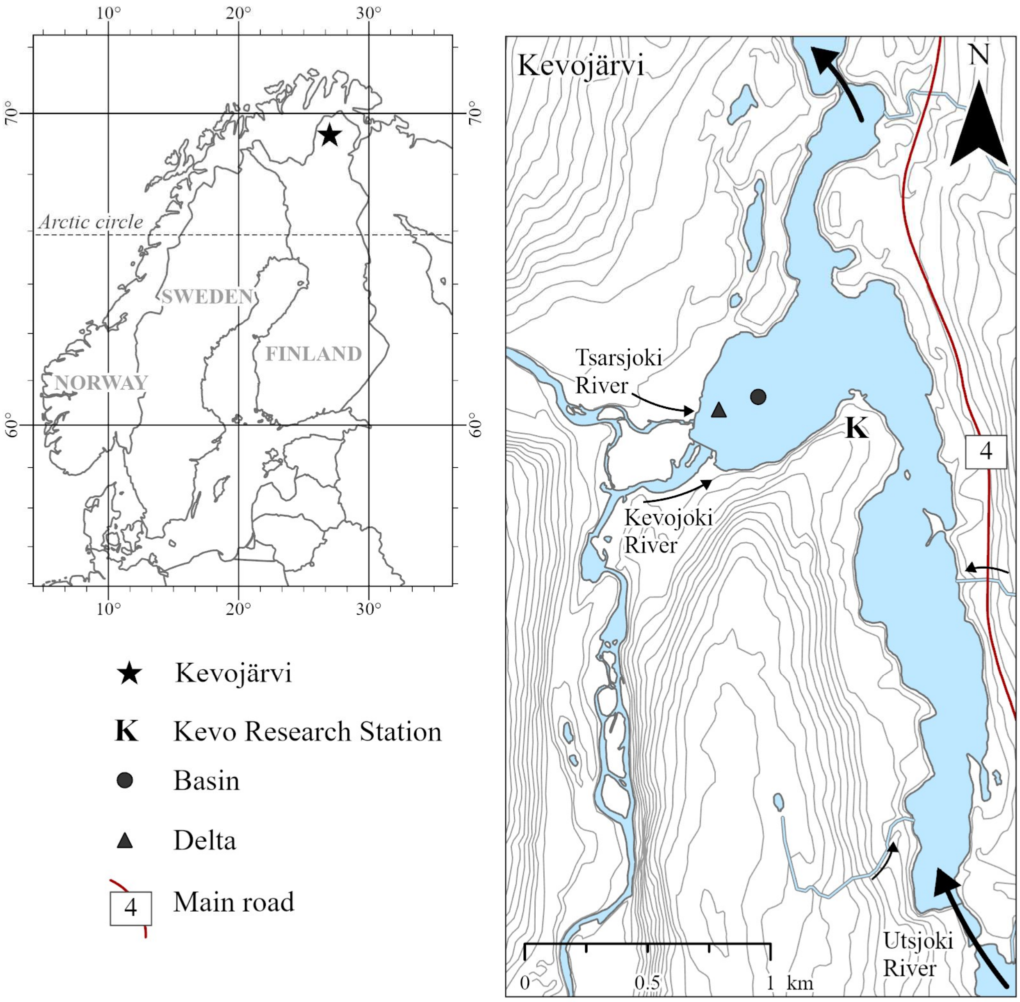

Figure 1. Location of the study site, Lake Kevojärvi (69º45′34’’N, 27º00′23’’E). Basin (circle) and delta (triangle) represent sediment trap locations. Data used for the Kevojärvi map on the right were obtained from Syke (2026; shorelines) and National land survey of Finland (MML, 2026; vector data consisting of elevation contours, roads, and stream networks).

Lake Kevojärvi catchment is part of the Kevo interlobate fell region (KEINF) and was completely under ice during the last glaciation (Palmu *et al.*, 2021). Therefore, the catchment is predominantly composed of glacial tills and the riversides contain glaciofluvial deposits (GTK, 2021). In addition to these, peat, exposed bedrock and blockfields are present throughout the area (GTK, 2010). Permafrost in the area occurs only sparsely in degrading palsa mires (Li *et al.*, 2020). Despite the traces of the last glacial period, the landscape is dominated by the preglacial Kevo canyon formed 70 million years ago, through which the Kevojoki river flows (Metsähallitus, 2017). The Western side of the catchment lies on the Lapland Granulite Belt, and quartz-feldspar paragneiss dominates on the Eastern side (GTK, 2022). Therefore, bedrock in the catchment area can be defined as felsic. Carbonate rocks are absent in the area (GTK, 2022). The variable topography of the catchment is characterized by low-lying river valleys and elevated fell areas. This variation creates sheltered areas where the tree lines of Scots pine may reach 200 m a.s.l. (Haltia *et al.*, 2021). However, species such as mountain birch and dwarf birch are abundant in elevated areas (Haltia *et al.*, 2021). Kevo Strict Nature Reserve is within the catchment of Lake Kevojärvi which emphasizes the minimal land use of the area. It is noteworthy that Lake Kevojärvi and its catchment are located within the Sámi homeland and form part of the reindeer herding area. Artificial surfaces (i.e., industrial, commercial and transport units) cover only 0.1% of the catchment area (Syke, 2014).

3 Materials and Methods

3.1 Sampling

Sediment trapping is a validated method for monitoring modern sedimentation, providing insight into the seasonality of sedimentation and sediment characteristics in both lacustrine and marine environments (Hargrave & Burns, 1979; Bloesch & Burns, 1980; Ojala *et al.*, 2013; Saarni *et al.*, 2021). When the seasonal accumulation pattern is studied, sediment trap is typically placed on the bottom of a deep basin where the continuous deposition most likely occurs (Ojala *et al.*, 2013; Saarni *et al.*, 2021). Sediment trapping can be the only method used for sample collection, as shown in the microplastic influx study by Saarni *et al.* (2021). However, sediment trapping is often used alongside sediment coring to confirm the annual nature of the laminated sediments observed in core samples (Dickman, 1985; Ojala *et al.*, 2013; Tylmann *et al*., 2017).

This thesis project was based on near-bottom sediment-trap monitoring, combined with water column monitoring, in Lake Kevojärvi. There were two moored sediment traps in the western basin of Lake Kevojärvi (Figure 1): one located at the deepest part of the basin (69°45,491’N, 26°59,895’E; depth: 35 m) and the other at the delta (69°45,462'N, 26°59,658'E; depth: 20 m). Main interest of the study was in the basin trap as it represents typical sediment accumulation zone, whereas the positioning of the delta trap was chosen for comparison and to gather information on the effect of spring flooding on the delta sedimentation. As in Saarni *et al.* (2021), both sediment traps consist of two polymethyl methacrylate (PMMA) plastic collector tubes (inner diameter 6.2 cm, height 40.5 cm, volume 1.2 l). The bottom of the cylindrical tube is made of stainless steel, and it is weighted to secure the upright position, which is also supported by the tube's articulated connection to the metal trap body. The tubes are positioned at a straight angle to each other, and a directing wing is in the middle of the trap body between two floats to keep the tubes equally positioned against the water currents (see Figure 2). Sinking polyester ropes connect the trap body to a subsurface buoy and an anchor weight. The trap body is fixed to the ropes 1 m above the lakebed to avoid disturbance from bottom sediments. A surface signal buoy is attached to the ropes of the sediment traps collected in autumn (i.e., summer samples).

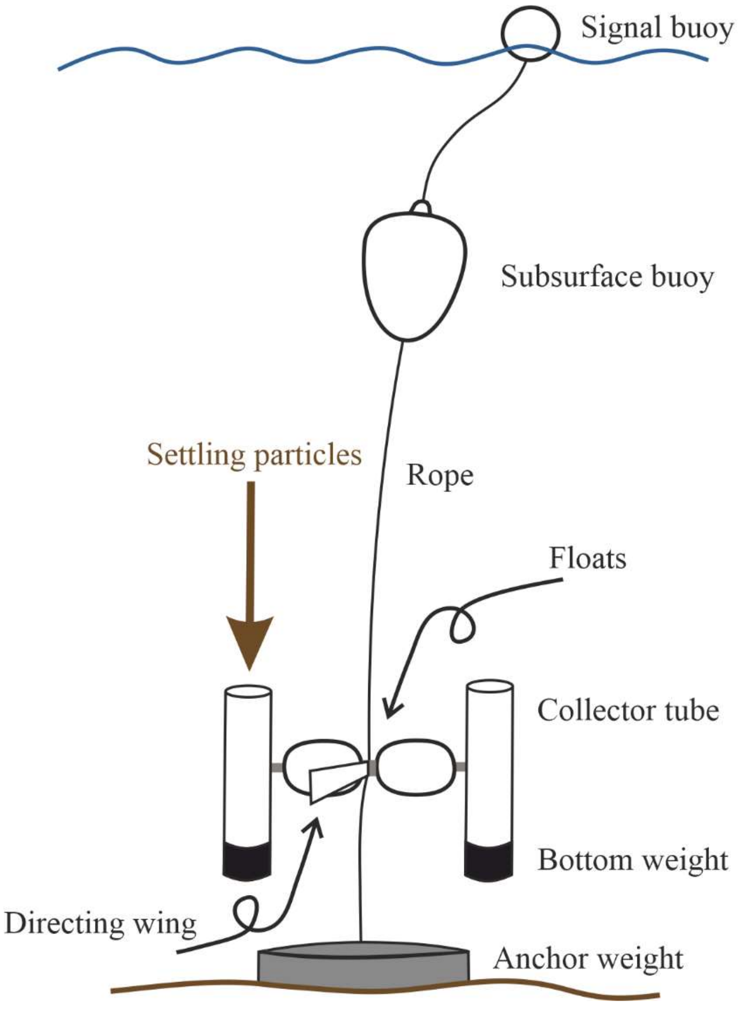

Figure 2. Simplified illustration of the moored sediment trap, based on Saarni *et al*. (2021). Signal buoy was only used during the summer sampling periods.

Sediment trap monitoring in Lake Kevojärvi began in April 2017 and is still on-going at the basin, but it was discontinued at the delta in autumn 2024. Material for this study was collected between September 2019 (for which the sediment traps were installed in June

2019) and October 2023 from the basin and the delta. The aim was to collect the samples three times per year from both study sites to detect the seasonal cycle of sedimentation. Target of this sampling cycle was to get samples from three seasons: spring, winter, and summer. Spring represents sedimentation during ice breakup, snowmelt, and spring flood, whereas the more stable seasons, winter and summer, represent sedimentation during ice cover and open water, respectively. Winter samples were collected between March and April just before snowmelt began, spring samples preferably in June right after the flood level had decreased, and summer samples between September and October just before ice formation.

The fieldwork was conducted from the Kevo Research Station of University of Turku. GPS points were used for locating the sediment traps. On site, sediment traps were collected from the boat (spring and summer samples), or from the ice (winter samples) by making a hole in it. A rake was used to catch the subsurface buoy set 1 m below surface and lift the traps from the lake bottom. If the sediment trap was not found under the ice using GPS points and the rake, it was located using sonar or a diver. After recovering the sediment trap, the collector tubes were detached from the sediment trap body, and the samples were poured into a white bucket made of food-grade polypropylene. Finally, the inner parts of the collector tubes were rinsed with distilled water to ensure the complete collection of the sample. The bucket was then sealed with a lid and labelled. The collector tubes were cleaned, and the sediment trap was reassembled, after which the sediment trap was reinstalled to the same location with caution to avoid disturbance of surface sediments. Samples were stored at the Kevo Research Station and then transported to the University of Turku where they were stored at 5 °C.

3.2 Sample preparation

Stored sample buckets contained collected sediments but also lake water from the collector tubes and distilled water from rinsing. Therefore, the water had to be removed before further analyses were made. Buckets were brought to the laboratory and left undisturbed to allow sediments to settle out of suspension before the water was removed from the samples manually using a glass syringe. After this, sediments were poured from the plastic buckets into the weighed and labelled crucibles. Complete sample recovery was ensured by rinsing the buckets with filtered distilled water. Wet weight was not measured because it did not represent the actual water content of sediments that accumulate on the lake bottom.

The crucibles were then covered with tin foil and frozen in a freezer overnight before drying in the freeze-dryer (Christ Alpha 1-4 LDplus; Figure 3). Vacuum pump was first warmed up for 20 minutes after which the drying phase consisting of the main drying (44h, -25 ºC, 0.63 mbar) and final drying (4h, -50 ºC, 0.40 mbar) was set to last for 48 hours in total. When the final drying was finished, the drying chamber was gently aeriated and lifted off the samples. Cold samples were then placed into the desiccators, and later the drying was repeated for the samples that still contained ice.

Figure 3. Sample preparation. Samples in the freeze-dryer (left), subsamples after loss on ignition (middle), and basin subsamples on the sample plate prior to μ-XRF analysis (right).

3.3 Sediment accumulation rate (SAR) and Loss on ignition (LOI)

The freeze-dried sediment samples were weighed in the crucibles, gently homogenized in the mortar and stored into 25 ml glass bottles. Weighing was conducted to obtain total sample mass and to calculate seasonal sediment accumulation rates (SAR). SAR was calculated for every sample based on the total dry mass (m_{dry}), as follows (Ojala *et al.*, 2013):

$$\mathrm{SAR} = \frac{m_{dry}}{A_{tot}t},$$

where A_{tot} represents the total collector tube area (m^2), and t is accumulation time in days.

Loss on ignition (LOI) is a widely accepted method for determining the organic matter (OM) content in sediments (Dean, 1974; Heiri *et al.*, 2001; Santisteban *et al.*, 2004; Bertrand *et al.*, 2024). The simple and cost-effective process of LOI is based on the combustion of OM, which begins approximately at 200 ºC and reaches completion at 550 ºC as reported in Dean (1974). The dry weight of the sediment sample lost in the combustion at 550 ºC represents the OM content (Dean, 1974). The LOI method described by Heiri *et al*. (2001) was used in this thesis. Freeze-dried sediment samples were first subsampled into labelled and weighed crucibles. Weighed subsamples were 0.5 g, 0.2 g, and 0.1 g for spring, summer, and winter, respectively. However, some exceptions were made due to the limited original sample sizes, particularly those representing winter season (0.063–0.383g). Ideally, the subsamples would have been of the same weight to avoid uncertainty as suggested in Heiri *et al*. (2001). Crucibles were then placed, with adequate spacing to allow air circulation (Figure 3), into the Nabertherm LT 15/11 muffle furnace, where they were combusted at 550 ºC for 4 hours. After this, the crucibles were let to cool in the desiccators before weighing. Unlike in Heiri *et al*. (2001), samples were not combusted in 950 ºC to measure carbonate content after weighing. This second step of ignition was omitted because the sediment samples in this study represent the catchment where carbonate minerals are absent. Therefore, in this study, dry weight of the residual after 550 ºC combustion represents the minerogenic matter (MM) content. Finally, LOI was calculated for each sample using the following equation (Heiri, *et al*., 2001), in which LOI_{550} is the LOI percentage at 550 ºC representing the OM content, DW and DW_{550} are the dry weights of the sample before and after ignition at 550 ºC, respectively.

$$LOI_{550} = \left(\frac{DW - DW_{550}}{DW}\right) 100\%$$

3.4 Micro-X-ray fluorescence (μ-XRF) spectrometry

Micro-X-ray fluorescence (μ-XRF) spectrometry is an analytical technique for determining elemental composition of various sample materials (e.g., solids, particles, and liquids) (Haschke, 2014). It is a non-destructive, high-resolution, and rapid technique with minimal sample preparation requirements, enabling the entire analysis process to be performed without compromising the samples (Haschke, 2014; Flude *et* al., 2017). Temporal variations in lacustrine environments can be studied through sediment geochemistry by utilizing μ-XRF technique, as in Ojala *et al.* (2013), Bonk *et al.* (2015), and Żarczyński et al. (2019).

In μ-XRF spectrometry, grounded in the principles of X-ray fluorescence (XRF), samples are exposed to radiation from an X-ray source (Haschke, 2014), most often an X-ray tube (Brouwer, 2010). By using μ-XRF, X-ray beam can be focused on a smaller sample area due to the instrumental additions to traditional XRF method enabling μm-scale measurements, and for example elemental mapping (Haschke, 2014; Mentzer, 2017). These primary X-rays cause excitation of atoms present in the sample (Weltje & Tjallingii, 2008). When the energy of the X-rays exceeds the core-electron binding energy, the electron is ejected from the atom (i.e., ionisation of an atom) (Potts & Webb, 1992; Brouwer, 2010). Almost instantly the remaining vacancy is filled with an electron from the higher energy levels releasing energy, which is emitted as secondary X-rays (i.e., fluorescence), unique to the atoms of specific element (Weltje & Tjallingii, 2008). In addition to fluorescence, the interaction between primary X-rays and sample causes Compton and Rayleigh scattering (i.e., incoherent and coherent scattering, respectively) (Brouwer, 2010). All three are dependent on the energy of the primary X-rays, as well as on the sample's composition, thickness, and density (Brouwer, 2010).

When the emitted X-rays reach the detector system, the characteristic energy (or wavelength) and intensity of the X-rays are measured (Brouwer, 2010). The detector system can be based on the direct measurement of the energy on the detector (Energy dispersive system, EDXRF), or the X-rays can be directed through a crystal, after which the wavelengths of the diffracted X-rays are measured on the detector (Wavelength dispersive system, WDXRF) (Brouwer, 2010). Based on the measurements, a spectrum is generated, from which the elemental composition of the sample can be determined. The peaks on the spectrum allow for the identification of the elements present in the sample, whereas the intensity, indicating the abundance of the elements in the sample, can be obtained from the area (EDXRF), or from the height (WDXRF) of the peaks (Brouwer, 2010).

In this study, an approach with minimal sample preparation for μ-XRF analysis was employed because the reuse of the subsamples was determined to be necessary due to the small initial sample sizes. For this purpose, a sample plate (10 cm x 14 cm) was cut from epoxy plate and 21 holes (diameter: 5.5 mm) were drilled for the samples (Figure 3). The subsamples, derived from the previously prepared samples, were gently compressed into the separate holes of the sample plate with a pestle, aiming for a flat sample surface. Sample holes were covered while individual samples were being prepared, and the sample surfaces were covered right after the preparation to prevent contamination. Before scanning, covers were removed, and the filled sample plate was sprayed with hairspray (light elements in the ingredients are not in the detection range) to ensure attachment of the samples.

Scanning was conducted on two separate days, first for the delta samples and then for the basin samples with an energy dispersive M4 Tornado (Bruker) µ-XRF spectrometer at the Geohouse, University of Turku. It is equipped with polycapillary X-ray optics, rhodium (Rh) anode and XFlash silicon drift detectors. The range for detection is from sodium (Na) to americium (Am). Prior to measurements, the warming of the X-ray tube (20 min) and instrument calibration with zirconium (Zr) are required. For the scanning, sample plate was attached to the controllable stage inside the measurement chamber. The spectrometer is connected to a PC with M4 Tornado software, through which the measurements in the chamber were operated, including instrumental control and monitoring of the sample positioning. In order to enable the detection of light elements that emit low-energy radiation, measurements were performed under vacuum (20 mbar), which prevents the radiation to be absorbed by air before reaching the detector (Brouwer, 2010; Bertrand *et al.*, 2024). The spectrometer was operated at a tube voltage of 50 kV and a current of 600 µA. Exposure time was set to 60 ms/pixel and scanning resolution was 100 µm. In addition to this, three basin samples (winter 2021–2022, spring 2022, and summer 2022) were scanned again with higher resolution (20 µm). Area analysis was used for this study with 100 µm pixel distance. Filters were not used. After the scanning, samples were removed from the plate, weighed and stored in separate beakers, which were sealed with laboratory film.

The collected data from each sample were analysed individually by using M4 Tornado software as a first step of data processing. Software generated a spectrum based on the scanned area, and performed peak search and identification based on its own database. Deconvolution was selected to separate possible overlapping peaks from each other (Brouwer, 2010). Interpretation of the peaks identified by the software was then carried out and only the elements relevant to the study (Al, Ca, Fe, K, Mg, Mn, Na, P, S, Si, Ti) were selected for further analysis. High peaks of Rh (from X-ray tube radiation) were excluded. After this Map result tab was opened to observe the elemental maps (i.e., 2d images of the selected elements), in which every pixel in the scanned area contains a full X-ray spectrum (Flude *et al.*, 2017). The brightness of a pixel represents the intensity of an element displayed on the map (Flude et al., 2017). However, these elemental maps only provide the first overview of the distribution and possible abundance (qualitative) of the element in the scanned area. Images of the different samples cannot be compared to each other. Because the scanned area was wider than the sample surface, a circle object (2036 pixels) was drawn inside the sample area by using the element image of Si due to its uniform distribution over the sample area and absence from the sample plate in each sample. This gave a results table showing the total intensity (counts per second, cps) of each element within the selected area, i.e., the region of interest (ROI) sum (Flude *et al.*, 2017). These were then exported to Excel. The same process was repeated to each sample, after which the result tables were combined into two datasets, delta and basin.

The intensities of these datasets are not directly comparable. Because the seasonal variations of sediment geochemistry (i.e., element variability between the samples), are of particular interest in this study, centered log-ratios (clr) of elements were calculated for each sample as suggested in Weltje *et al.* (2015), and utilized by Bertrand *et al.*, (2024) and Lincoln *et al.*, (2025). This enables the analysis of the data with multivariate statistical analysis (Weltje *et al.*, 2015). Clr was calculated for each element with the following equation (Weltje *et al.*, 2015), in which x_i is the intensity (cps) of the element and g(x) is the geometric mean, where D is the number of the selected elements.

$$\mathrm{clr}(x_i) = \ln\left(\frac{x_i}{g(x)}\right)$$

Where:

$$g(x) = \left(\prod_{i=1}^{D} x_i\right)^{\frac{1}{D}}$$

The sums of negative and positive dimensionless clr values were calculated to each sample to ensure the correctness of clr calculations (i.e., sum equal to zero) as in Bertrand *et al*., (2024). However, selected elemental ratios (Si/Al, Si/Ti, Si/K, Ti/Al, K/Al, and Mn/Fe) were calculated from the raw geochemical data (i.e., µ-XRF element intensities) to explore potential indicators of temporal variations in the lake and its catchment, as suggested in Bertrand *et al.* (2024). Natural logarithm (ln) was taken from the ratios to achieve better visual detectability of seasonal trends.

In order to visualize the geochemical data and highlight the relationships between the elements (Al, Ca, Fe, K, Mn, P, S, Si, and Ti) and sampling periods (summer, winter, and spring), principal component analysis (PCA) was conducted in PAST 5.3 software (Hammer *et al*., 2001) on clr-transformed geochemical data, separately for the basin (n = 13) and delta (n = 10). A variance-covariance matrix was used because of the unitless clr-transformed values. Based on the default settings and user-selected options, PCA was re-run in Python 3.11.9 using Pandas, NumPy, Matplotlib, and Scikit-learn libraries for better visual flexibility when creating PCA biplots. Scripts were drafted using Jupyter Notebook, after which ChatGPT (OpenAI) was used as an assistant in tasks such as debugging and generating code snippets. Delta sample winter 2020–2021 (year in figures) included spring 2021 sample and was therefore excluded from the analysis. However, it was projected as a supplementary variable onto the biplot based on the analysis of the other delta samples.

3.5 Hydrological data

Hydrological data and water column monitoring is required to assess the prevailing conditions in water column during sedimentation which alter, for example, sediment composition and flux. Water column monitoring was conducted alongside the moored sediment trap at the basin as its own mooring, which consisted of a bottom weight, sinking ropes and buoys similar to those in sediment traps. Five HOBO loggers (Onset Computer Corporation) were attached to the sinking rope at 6-m intervals from 6 to 30 m, to record hourly water temperature. In addition, YSI EXO2 Multiparameter Sonde (Xylem Inc.) was positioned to monitor the lake bottom conditions at the same depth as the basin sediment trap was mounted (34 m), 1 m above the lakebed to avoid disturbance from the sediments. It records multiple parameters at an hourly resolution, including water temperature (°C), pH, conductivity (µS/cm), dissolved oxygen (DO; mg/l), turbidity

(FNU), and depth (m) calculated from pressure. Specific conductance (µS/cm; normalized to 25 °C), total dissolved solids (TDS; mg/l), and salinity (PSU) were derived automatically from the measured temperature and conductivity values.

Water temperatures from different depths were required to construct a thermal structure of the water column, enabling the identification of thermal stratification patterns and mixing events, as well as the determination of their onset and duration. Oxygen depletion here comprises anoxia (DO < 0.5 mg/l) and hypoxia (DO < 2 mg/l) in accordance with Jansen *et al*. (2024). In addition to DO, sediment geochemistry is also altered by the temperature and pH of the bottom waters. Turbidity was recorded as an indicator of suspended particulate matter potentially available for sedimentation, whereas dissolved solids were monitored to characterize water-sediment interactions. The measurements of specific conductance, TDS, and salinity represent dissolved solids, reflecting conductive ions, organic and inorganic dissolved solids, and dissolved inorganic solids, respectively. Non-representative measurements, for example those recorded during instrument maintenance, were identified and excluded based on depth and comparisons of temperature measurements.

The following hydrological data were obtained from the Hertta database of Finnish Environment Institute (Syke, 2024). Water column monitoring was completed with Lake Kevojärvi's surface water temperatures (69.75659ºN, 27.00316ºE; 20 cm below surface) and ice cover observations. The annual ice cover duration was calculated based on the ice cover observation dates of stable ice cover and ice-free conditions. River discharge data, indicating temporal patterns and intensity of sediment transport (Ojala *et al.*, 2013), were not available for Tsarsjoki or Kevojoki rivers that flow into the western basin of Lake Kevojärvi. For this reason, daily discharge data were obtained from Utsjoki Patoniva measuring station located 3 km downstream to the north from Lake Kevojärvi, between the lakes Jomppalanjärvi and Jorpajärvi (69.78366ºN, 26.99953ºE).

3.6 Meteorological data

There are two weather stations (69.8ºN, 27ºE) owned by Finnish Meteorological Institute (FMI) in the vicinity of Lake Kevojärvi, Utsjoki: Kevojärvi (76 m a.s.l) and Kevo (107 m a.s.l.) (FMI, 2024b). According to FMI, both stations represent well the weather conditions of the river valleys in the area, which also applies to Lake Kevojärvi and its catchment (FMI, 2024b). Due to the low-lying position of Kevojärvi station, it is prone to flooding, which caused a data gap in 2020 affecting all three sampling periods. A continuous air temperature record was needed to detect seasonality, and therefore all meteorological data were obtained from Kevo station. Meteorological observations were retrieved from FMI's open data service (FMI, 2024a) for 6/2019–11/2023, including daily and monthly mean air temperatures (°C), precipitation sums (mm; daily and monthly), and daily snow depth (cm).

4 Results

4.1 Temporal coverage and sample characteristics

This study was based on the samples that cover the period between 17 June 2019 and 11 October 2023, during which a total of 24 samples were collected, comprising 13 samples from the basin and 11 from the delta (see Appendix 1 and 2, respectively). Each sample represents a certain sampling period, which are named after three seasons: summer, winter and spring. The date on which the sediment trap was set defines the year of the sampling period, for example, sample that was set in 9/2019 and was collected in 4/2020, represents winter 2019–2020. When the collection of the sediment traps was conducted as intended, the longest sampling period was winter, and the shortest was spring. Each sample consisted of material from two collector tubes, except for summer 2020 delta sample, which included material from a single collector tube.

In spring 2020, recovery of the samples was affected by extreme floods. Therefore, separate winter 2019–2020 and spring 2020 samples were not collected from the delta. In addition to this, spring 2020 sample was not collected from the basin in June but in the beginning of August. On the same date, delta sample, now consisting of the sampling periods of winter 2019–2020 and spring 2020, was recovered. Late collection date led to a short accumulation period (63 days) for summer 2020 samples. In 2021, summer sample was not collected from the delta. In addition, at both sites in 2022, spring samples were collected on June 20, but the sediment traps were set again on June 29, causing a short break between the spring and summer sampling periods. Based on the observations of the stored samples, winter samples were the most homogeneous and consisted of fine material. Spring samples were the most heterogeneous consisting of variable grain sizes and visible organic fragments of terrestrial origin, such as birch leaves. In addition, organic (i.e., muddy) odour, brownish excess water, and rusty staining inside the buckets distinguished spring 2022 samples from other samples, which were mostly odourless with clear, or slightly greyish excess water.

4.2 Sediment composition and fluxes

Sampling period durations (days), dry sample amounts, LOI results, and fluxes are listed in Table 1 (basin) and 2 (delta). All subsample sizes can be found in Appendix 2. Sediment accumulation rates clearly followed the pattern of the three sampling periods as shown in

Figure 4 and 5. Despite the length of the sampling periods, spring samples had the highest SAR, whereas winter samples had the lowest SAR. For the corresponding samples, spring accumulation rates were higher at the delta. Throughout other sampling periods, rates were generally higher at the basin, except in winter 2020–2021, when they were the same order of magnitude. It is noteworthy that the lowest SAR in spring was higher than the maximum rates in summer, and the lowest SAR in summer was higher than the maximum rates in winter.

Table 1. Basin sampling periods, sediment composition and fluxes

Sampling period	t (days)	Dry mass (g)	SAR ($g\ m^{-2}\ day^{-1}$)	LOI (%)	OM flux ($g\ m^{-2}\ day^{-1}$)	MM flux ($g\ m^{-2}\ day^{-1}$)
summer 2019	101	0.852	1.397	35.1	0.490	0.907
winter 2019–2020	194	0.295	0.252	36.1	0.091	0.161
spring 2020*	120	13.069	18.037	15.4	2.778	15.259
summer 2020**	63	0.414	1.088	33.2	0.361	0.727
winter 2020–2021	177	0.319	0.298	36.9	0.110	0.188
spring 2021	77	2.272	4.887	37.4	1.828	3.059
summer 2021	102	1.303	2.116	38.5	0.815	1.301
winter 2021–2022	188	0.249	0.219	40.2	0.088	0.131
spring 2022	77	5.955	12.808	42.4	5.431	7.378
summer 2022	103	0.907	1.458	38.5	0.561	0.898
winter 2022–2023	166	0.384	0.383	36.0	0.138	0.245
spring 2023	86	1.399	2.694	38.6	1.041	1.653
summer 2023	114	1.266	1.839	40.5	0.745	1.094

Sampling period longer * or shorter ** than intended

Table 2. Delta sampling period durations, sediment composition and fluxes

Sampling period	t (days)	Dry mass (g)	SAR ($g\ m^{-2}\ day^{-1}$)	LOI (%)	OM flux ($g\ m^{-2}\ day^{-1}$)	MM flux ($g\ m^{-2}\ day^{-1}$)
summer 2019	101	0.578	0.948	27.4	0.260	0.688
winter 2019–2020*	314	22.141	11.678	10.4	1.215	10.463
summer 2020**	63	0.112	0.589	38.1	0.224	0.365
winter 2020–2021	178	0.328	0.305	34.6	0.105	0.200
spring 2021	76	3.523	7.677	26.4	2.027	5.650
winter 2021–2022	189	0.063	0.055	37.4	0.021	0.035
spring 2022	76	19.126	41.678	20.4	8.502	33.176
summer 2022	103	0.617	0.992	35.5	0.352	0.640
winter 2022–2023	166	0.196	0.196	29.6	0.058	0.138
spring 2023	86	5.717	11.009	26.6	2.929	8.081
summer 2023	114	0.874	1.270	31.4	0.399	0.871

Sampling period longer * or shorter ** than intended

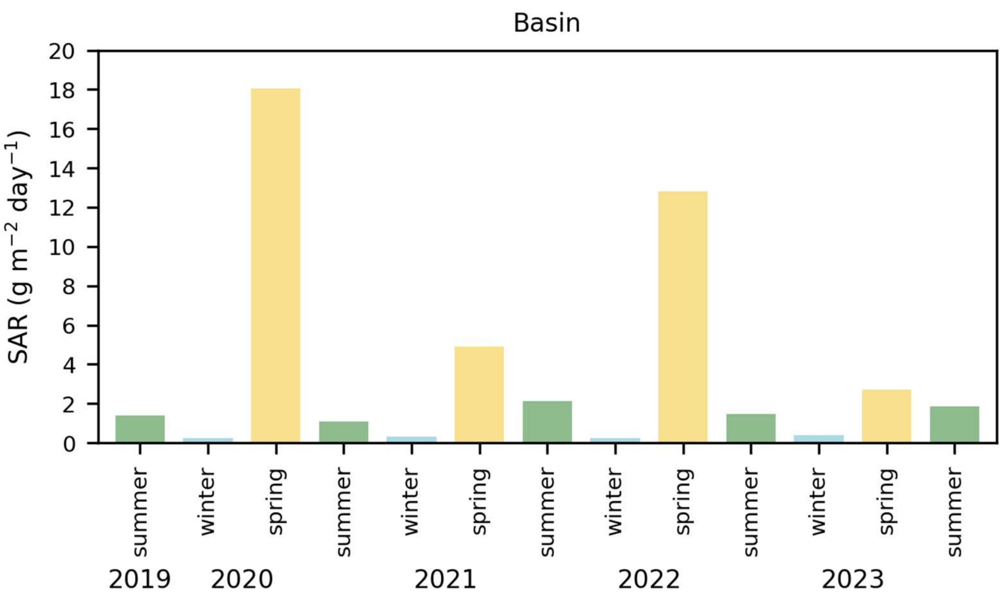

Figure 4. Sediment accumulation rates (SAR) at the basin representing the three sampling periods spring (yellow), summer (green), and winter (blue) during which the year changes. Note that the spring (prolonged) and summer 2020 (shorter) differ from the typical sampling durations.

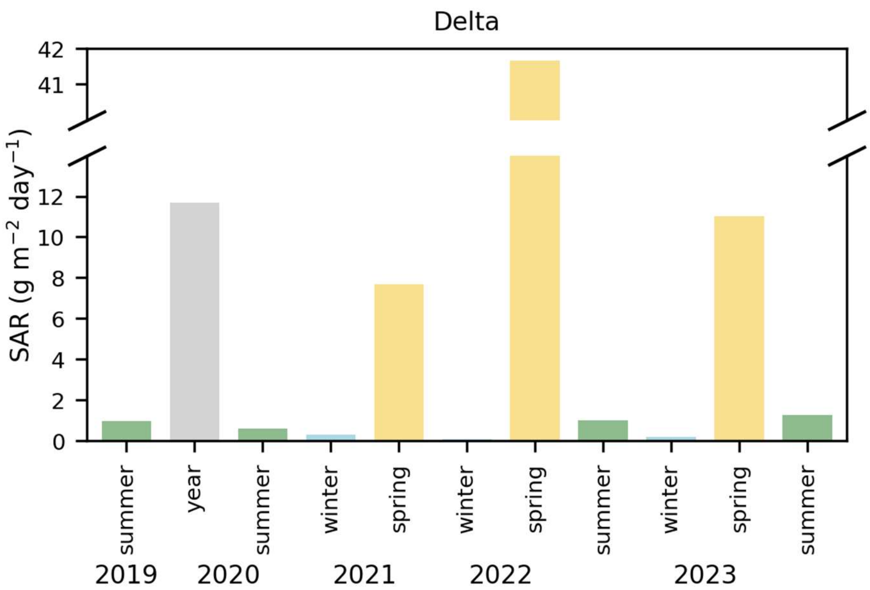

Figure 5. Sediment accumulation rates (SAR) at the delta representing the three sampling periods spring (yellow), summer (green), and winter (blue) during which the year changes. Year (grey) is the prolonged winter 2019–2020 sampling period. Note that also summer 2020 differs from the typical sampling duration representing only the latter part of the summer period.

Most of the annual sediment accumulation occurred in spring (see the dry masses in Table 1 and 2). Spring SAR at the basin was the highest in 2020 (18.037 g m^{-2} day^{-1}) and the lowest in 2023 (2.694 g m^{-2} day^{-1}), whereas at the delta, it was the highest in 2022 (41.678 g m^{-2} day^{-1}) and the lowest in 2021 (7.677 g m^{-2} day^{-1}). Summer had a modest contribution to the annual accumulation. SAR was the highest in 2021 (2.116 g m^{-2} day^{-1}) and 2023 (1.270 g m^{-2} day^{-1}), at the basin and the delta, respectively. At both sites, summer SAR was the lowest in 2020 (basin: 1.088 g m^{-2} day^{-1}; delta: 0.589 g m^{-2} day^{-1}). Winter had a minor contribution to the annual accumulation. SAR was the highest at the basin in 2022 (0.383 g m^{-2} day^{-1}), and at the delta in 2020 (0.305 g m^{-2} day^{-1}). Winter SAR was at its lowest in 2021 at both sites (basin: 0.219 g m^{-2} day^{-1}; delta: 0.055 g m^{-2} day^{-1}).

In this study, LOI at 550 ºC represents the organic matter content in samples, and the remaining percentage is considered minerogenic matter (MM) content. Organic and minerogenic content are expressed as percentages. To avoid misleading results, basin spring 2020 and delta winter 2019–2020 (i.e., year in figures), the samples with the lowest OM content (15.4% and 10.4%, respectively), were omitted from mean and median calculations due to their prolonged sampling periods. The overall OM content was higher at the basin (n = 12; median 37.9%; mean 37.8%) than at the delta (n = 10; median 30.5%; mean 30.7%). OM content did not follow the seasonal variation as seen in Figure 6 and 7. Only at the delta, spring samples differed from other sampling periods by their lower OM content, with the highest measured in 2023 (26.6%) and the lowest in 2022 (20.4%). At the basin, OM content in spring was the highest in 2021(42.4%) and the lowest in 2022 (37.4%). For summer, OM content at the basin was the highest in 2023 (40.5%) and the lowest in 2020 (33.2%). At the delta, in contrast, OM content was the highest in 2020 (38.1%) and the lowest in 2022 (27.4%). Winter samples had the highest OM content in 2021(basin: 40.2%; delta: 37.4%) and the lowest in 2022 (basin: 36.0%; delta: 29.6%) at both sites.

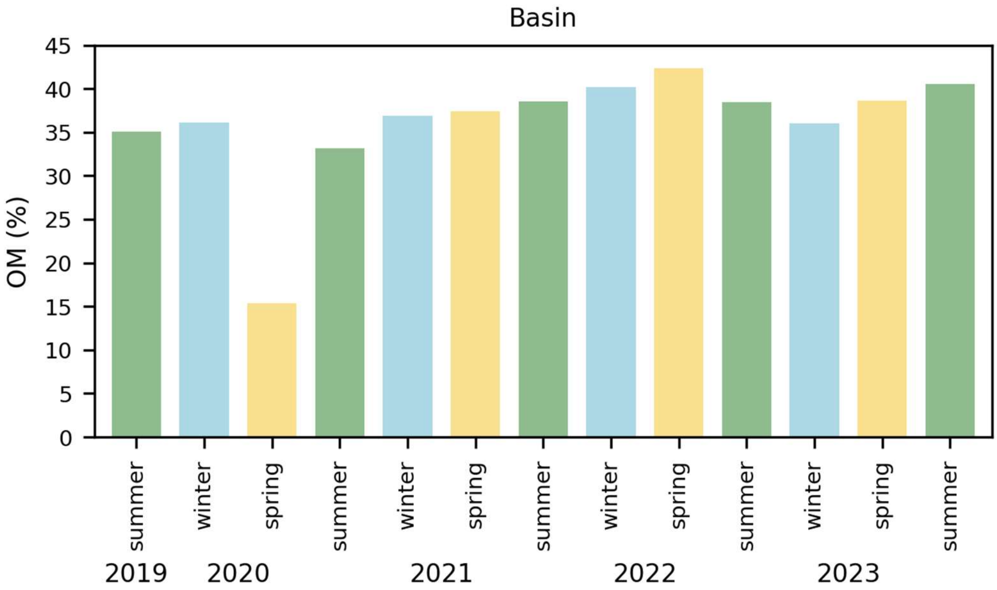

Figure 6. Organic matter content (OM) of the basin sediment samples based on the loss on ignition (LOI). Each sample represents their sampling period: spring (yellow), summer (green), and winter (blue) during which the year changes. Note that the spring (prolonged) and summer 2020 (shorter) differ from the typical sampling durations.

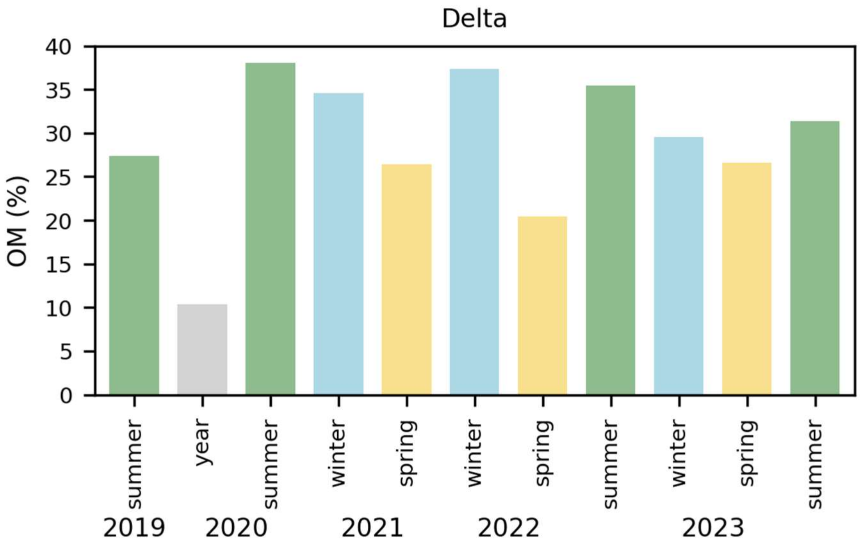

Figure 7. Organic matter content (OM) of the delta sediment samples based on the loss on ignition (LOI). Each sample represents their sampling period: spring (yellow), summer (green), and winter (blue) during which the year changes. Year (grey) is the prolonged winter 2019–2020 sampling period. Note that the duration of the summer 2020 (shorter) differs from the typical sampling durations.

Organic and minerogenic fluxes shared the timing of their highest and lowest values with total SAR, following a similar seasonal pattern. The only exception occurred at the basin, where the highest organic flux was in spring 2022 (5.431 g m^{-2} day^{-1}), rather than in spring 2020. At the basin, the lowest organic flux was 0.088 g m^{-2} day^{-1}. Minerogenic flux varied between 0.131 g m^{-2} day^{-1} and 15.259 g m^{-2} day^{-1}. At the delta, organic flux varied between 0.021 g m^{-2} day^{-1} and 8.502 g m^{-2} day^{-1}, and the minerogenic flux range was 0.035–33.176 g m^{-2} day^{-1}. Organic and minerogenic fluxes were highest in spring, followed by summer, and the lowest in winter. Minerogenic flux was always higher than the corresponding organic flux at both sites. All the organic and minerogenic fluxes from both sites are listed together with SAR values in Table 1 (basin) and 2 (delta).

4.5 Sediment geochemistry

Total intensities (cps) were derived as ROI sums for each selected element (Al, Ca, Fe, K, Mg, Mn, Na, P, S, Si, Ti) in subsamples representing the samples from both sampling sites. Na and Mg showed near zero intensities and were not considered further. Three basin samples (winter 2021–2022, spring 2022, and summer 2022) were scanned also with higher resolution (20 µm) and their elemental maps are presented in Figure 8. The relative geochemical composition of each sample scanned with 100 µm resolution was obtained from the clr transformed values of the intensities (cps). The sum of clr values for each sample was equal to zero. Total intensities, clr values, and sample-specific clr sum results are provided in Appendix 3 (basin) and 4 (delta). Positive clr values mean that the element is more abundant than average in the sample, i.e., above the geometric mean. Fe, Mn, Si, and Ca had a positive range, whereas K, Al, S, and P had a negative range, and Ti had mainly negative values. The clearest seasonal trends based on the sampling periods were associated with spring as drops and peaks in clr-values of the redox-sensitive elements (Fe, Mn) and the lithogenic fraction (Ti, Al, K), respectively. These trends were also shown in spring 2020 (basin) and year 2020-2021 (delta) despite their prolonged sampling periods. Clr-ranges of individual elements and seasonal trends can be observed in Figure 9 (basin) and 10 (delta).

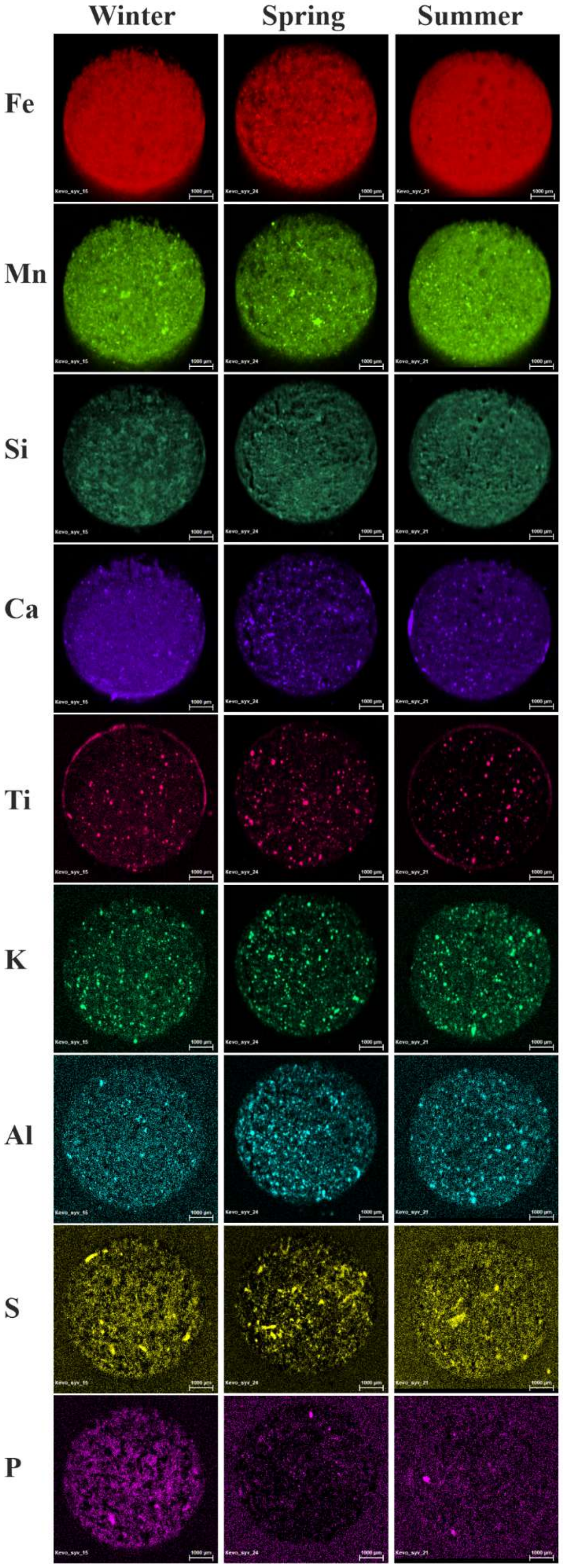

Figure 8. Elemental maps of the three μ-XRF basin subsamples (winter 2021–2022, spring 2022, and summer 2022) based on the scanning with higher resolution (20 μm).

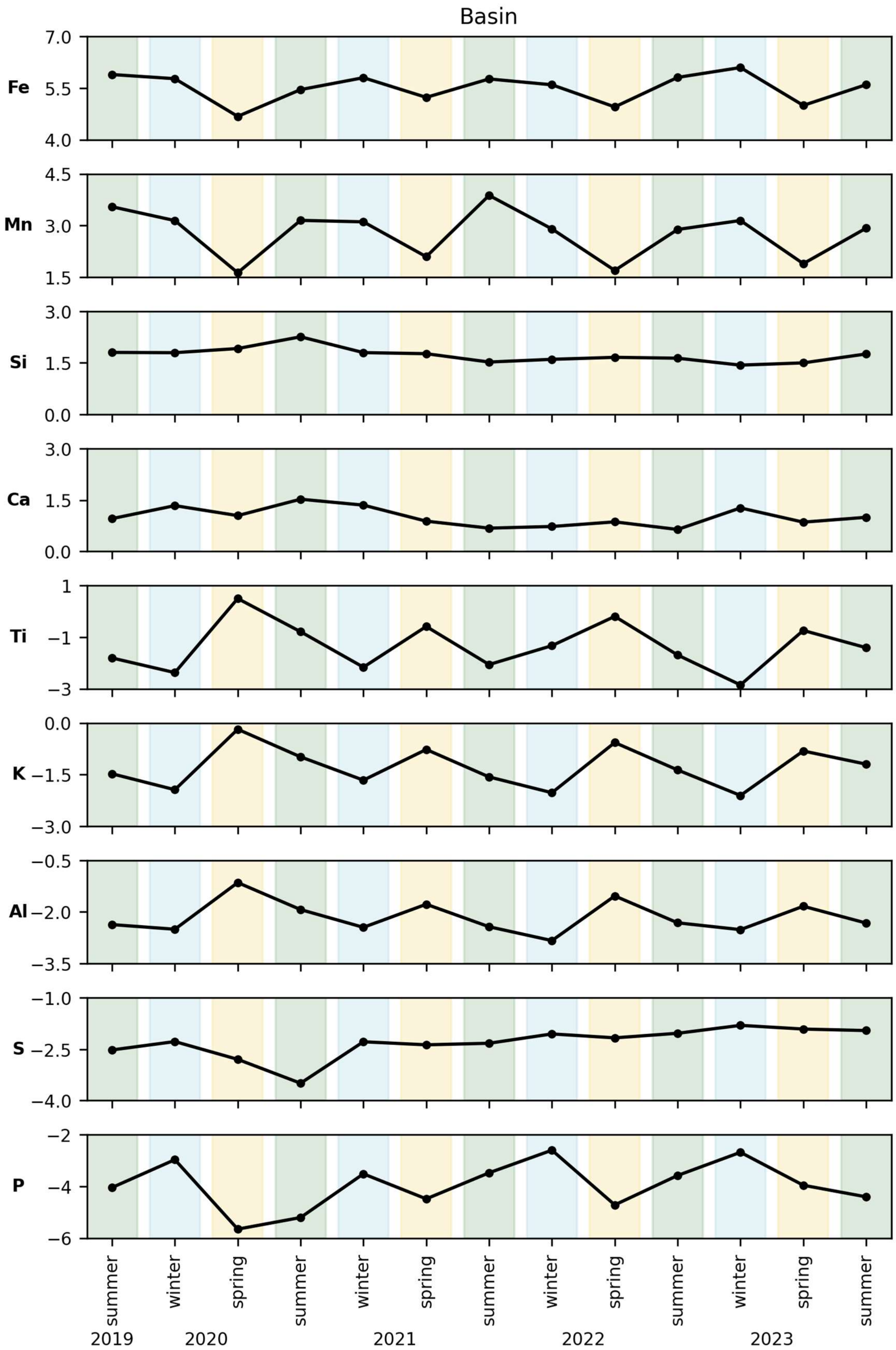

Figure 9. Clr-transformed geochemical data for basin. Note: vertical scale is 3 for most and 4 for Ti and P. Spring 2020 sampling period was prolonged, and therefore summer 2020 represents only the latter part of the intended summer sampling period.

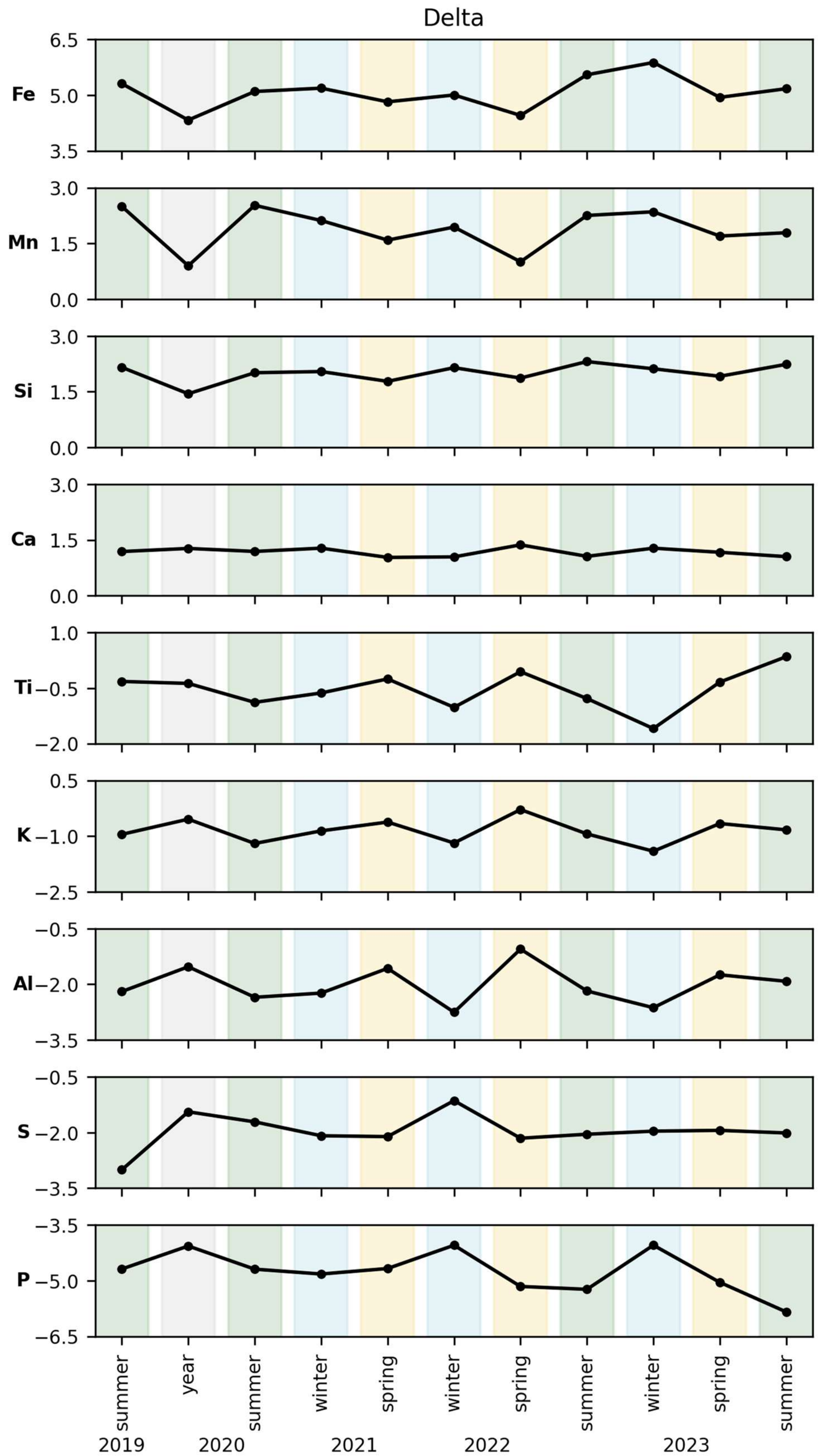

Figure 10. Clr-transformed geochemical data for delta. Vertical scale is 3 for all the elements. Year (grey) is the prolonged winter 2019–2020 sampling period. Summer 2020 represents only the latter part of the intended summer sampling period.

Elemental ratios for Si/Al, Si/Ti, Si/K, Ti/Al, K/Al, and Mn/Fe, i.e., natural logarithms of the µ-XRF element intensity (cps) ratios, are provided in Appendix 3 (basin) and 4 (delta). Figure 11 (basin) and 12 (delta) show the elemental ratios across the sampling periods. The clearest seasonal pattern was the decrease in Si ratios in spring samples. Corresponding trend was visible in Mn/Fe ratios representing the basin (Figure 11).

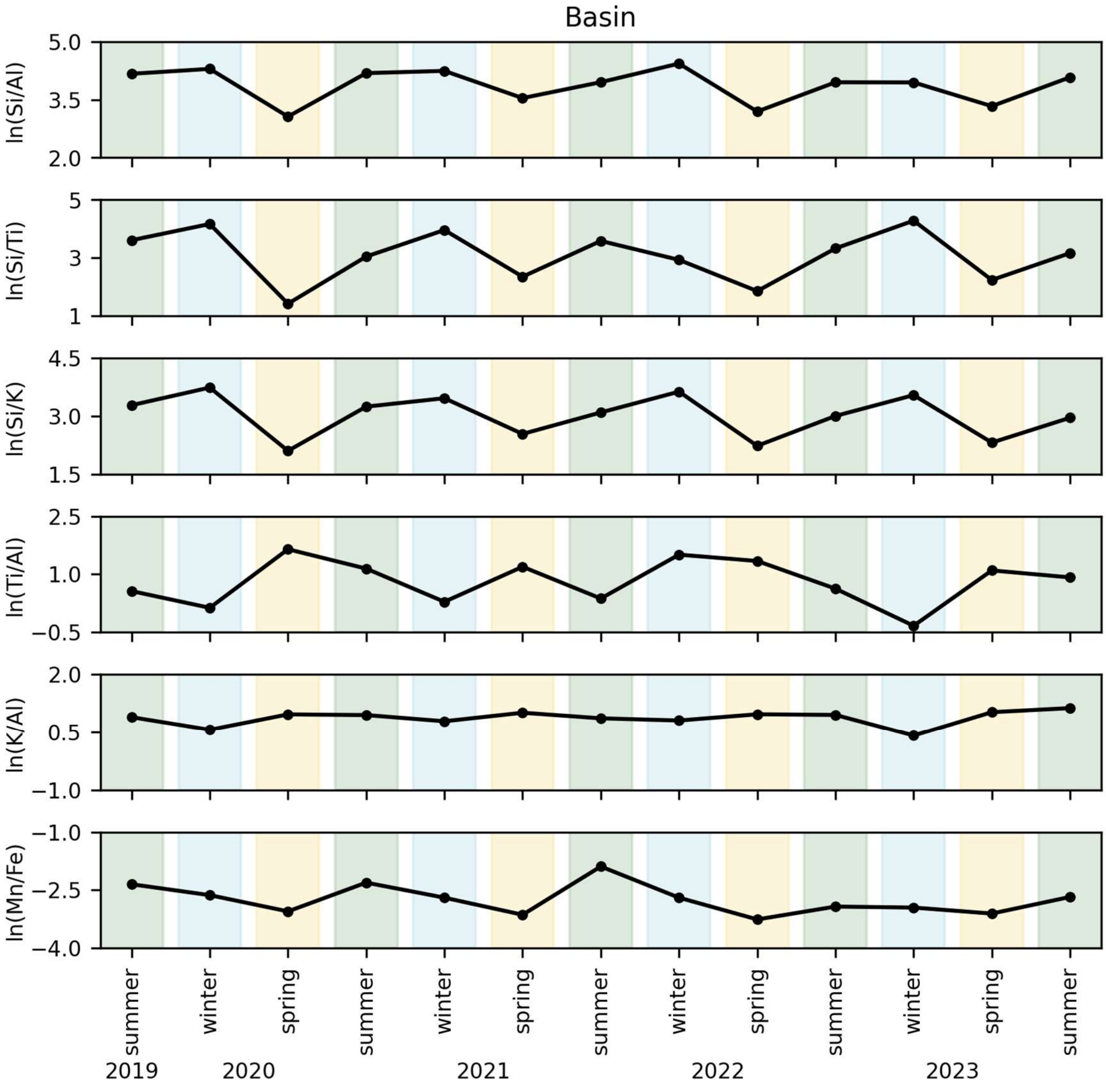

Figure 11. Natural logarithms of the µ-XRF element intensity ratios for the basin. Note: vertical scale is 3 for most and 4 for ln(Si/Ti). Spring 2020 sampling period was prolonged, and therefore summer 2020 represents only the latter part of the intended summer sampling period.

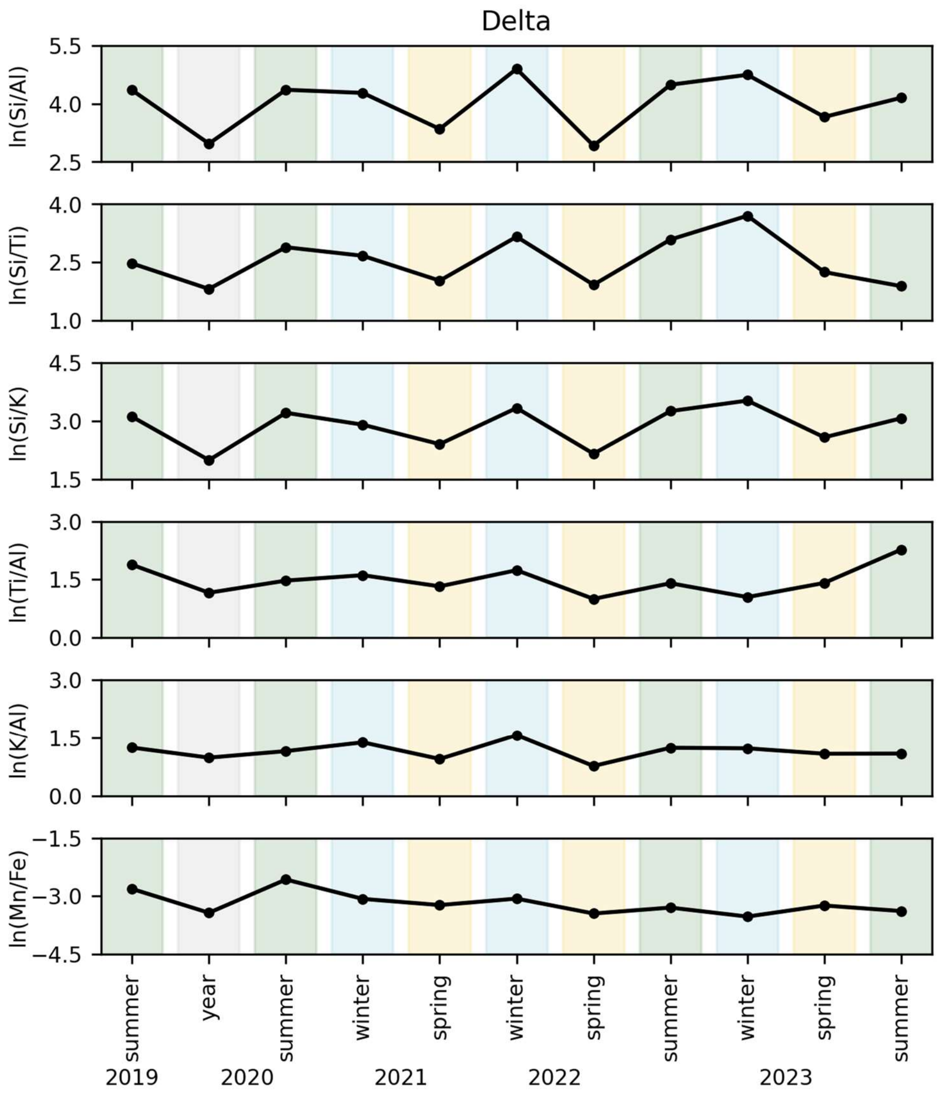

Figure 12. Natural logarithms of the µ-XRF element intensity ratios for the delta. Vertical scale is 3 for all. Year (grey) is the prolonged winter 2019–2020 sampling period. Summer 2020 represents only the latter part of the intended summer sampling period.

The first two principal components of PCA explained most of the variance in the clr transformed geochemical data: 78.8% (PC1) and 14.0% (PC2) for basin, and 62.8% (PC1) and 19.4% (PC2) for delta. As seen in the biplots (Figure 13 and 14) spring was distinguished as its own group from other sampling periods, whereas summer and winter resembled each other. Fe and Mn showed an inverse relationship to Al and K (and Ti at the basin), which were associated with spring at both sites. PCA results are summarized in Appendix 5 (basin) and 6 (delta).

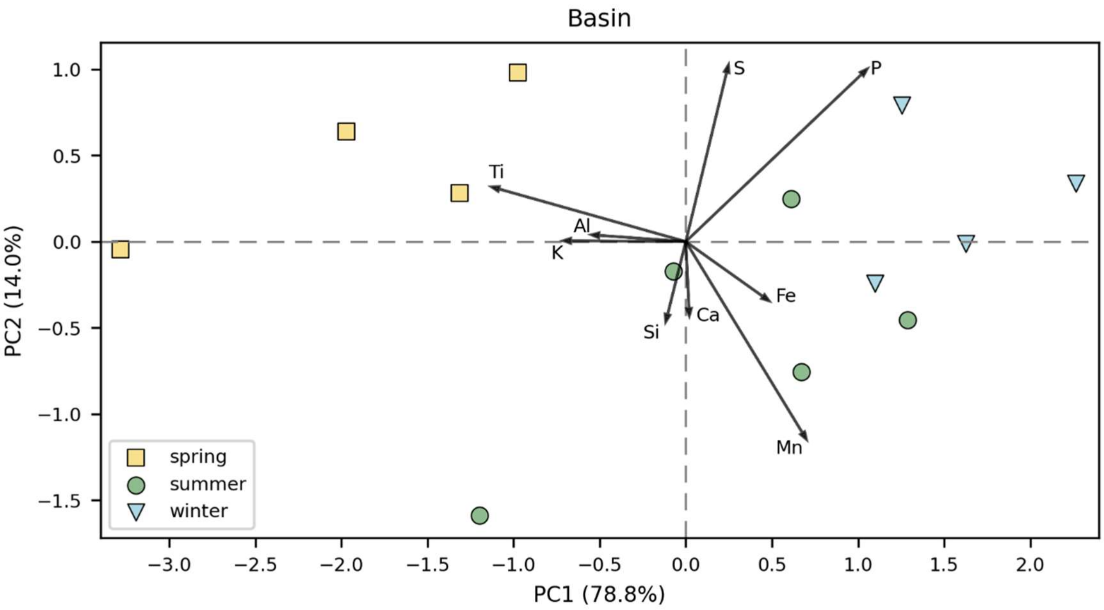

Figure 13. Study site basin. PCA biplot of the clr-transformed geochemical data (loadings; arrows) and the individual samples (scores) categorized by the sampling periods representing spring (yellow squares), summer (green circles), and winter (blue triangles).

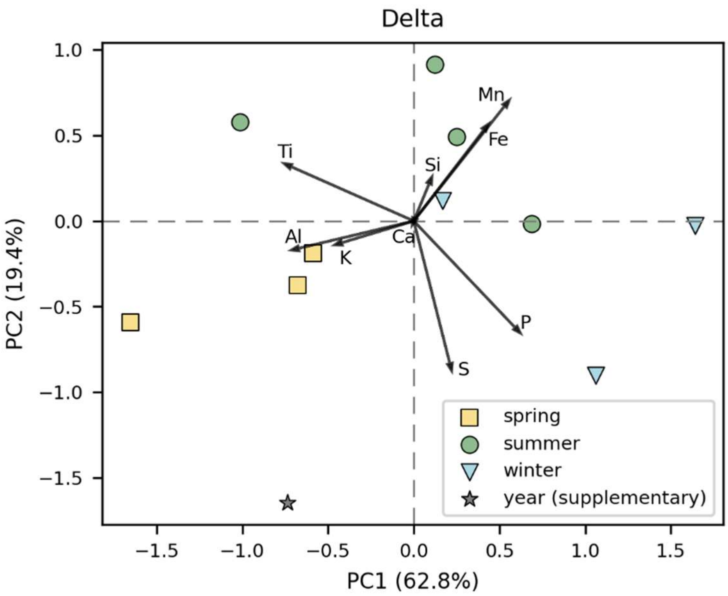

Figure 14. Study site delta. PCA biplot of the clr-transformed geochemical data (loadings; arrows) and the individual samples (scores) categorized by the sampling periods representing spring (yellow squares), summer (green circles), and winter (blue triangles). Year (i.e., the prolonged winter 2019–2020 sampling period) was excluded from the PCA analysis and plotted afterwards as a supplementary variable (grey star).

4.6 Hydrological conditions

Surface water temperature was measured only during the open water periods (see Figure 15). Over the study period, the mean surface water temperature was 11.3 °C (n = 676; range: 2.10–19.80 °C). Bottom-water temperature ranged from 1.4 to 12.5 °C, with a mean of 5.2 °C. Interannual variations and seasonal trends in thermal structure across the study period can be observed in Figure 15. Thermal stratification was formed every summer, except in 2020, and it persisted until the overturn in September. Periods of weak thermal stratification were also detected in 2020 but those were followed by mixing throughout the summer months (recorded in spring and summer 2020 sampling periods). The maximum surface-to-bottom temperature difference was observed in summer 2022, whereas the earliest autumn overturn occurred in September 2023. The latest overturn was detected in 2019, when cooling water column remained isothermal until reaching 4 °C (see isoline in Figure 15) in October, after which inverse stratification began to form. According to the sampling periods, the earliest onset occurred in October 2023 (note that winter 2023–2024 was beyond the study period). The latest onset was observed in winter 2021–2022 on October 31, which was three weeks later than in 2023. Spring overturn marked the breakdown of the inverse stratification, occurring earliest in mid-May (spring 2023 and 2022) and latest in late May (spring 2020). The initially isothermal water column warmed and became thermally stratified between late May and early June, with the earliest onset in spring 2022 and the latest in spring 2023. Detailed periods of thermal and inverse stratification are listed in Appendix 7.

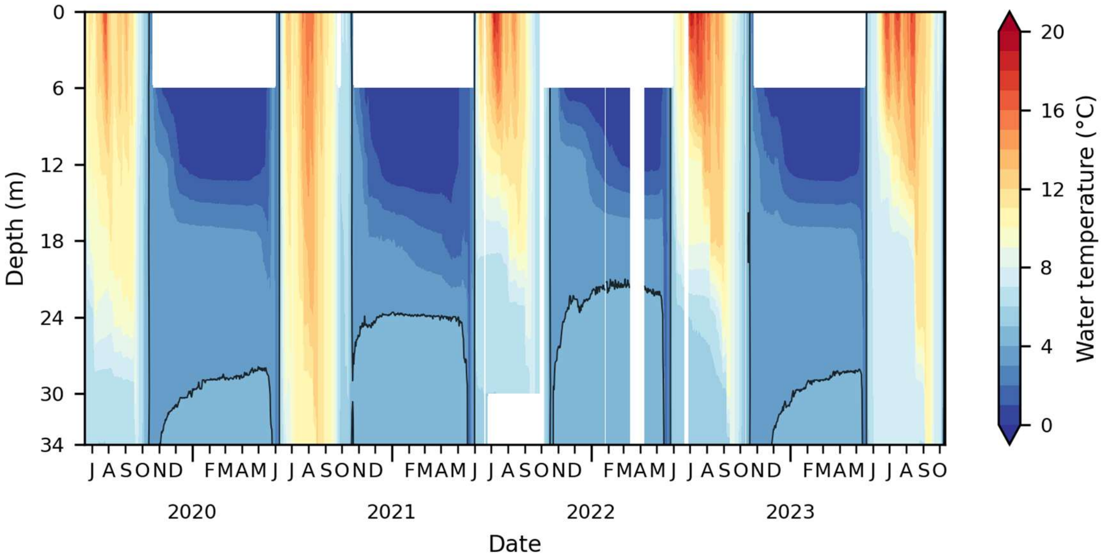

Figure 15. Contour plot of water temperature linearly interpolating 0.25 m vertical intervals based on the surface temperature from 20 cm below surface (Syke, 2024) represented here as 0 m, HOBO logger temperatures from 6, 12, 18, 24, 30 m, and EXO2 sonde bottom-water temperatures from 34 m. Daily means were used instead of the monitored hourly temperatures for better visual clarity. Black line is a 4 °C isotherm. White areas are data gaps. At the surface, this is due to the winter ice cover.

Hourly monitored water temperature (also in Figure 15), DO, pH, turbidity, specific conductance, salinity, TDS, and depth representing the bottom-water conditions at the basin (34,723 observations each), together with the daily discharge data obtained from Patoniva station (Syke, 2024) can be found in Figure 16. No EXO2 data were collected in summer 2021. As can be observed in Figure 16, DO ranged from 0 to 13.8 mg/l (negative values were treated as 0 mg/l; mean DO: 3.6 mg/l). Mean DO ranges for summer, winter, and spring sampling periods were 3.1–8.7 mg/l (summer 2019; 2020), 1.9–2.7 mg/l (winter 2021–2022; 2022-2023), and 4.6–5.5 mg/l (spring 2021; 2022). Stable periods of bottom-water temperature were followed by decreasing DO levels, which stabilized at 0 mg/l under steady thermal conditions in summer and winter.

As the transition towards oxygen depletion was gradual, continuous periods of hypoxia and anoxia were considered to have started when the daily mean DO dropped below 2 mg/l and 0.5 mg/l, respectively. During summers with continuous thermal stratification, hypoxia was reached in July. The onset of anoxic period ranged from mid-July (2022) to early August (2019). In addition, a brief, 5-day anoxic period was detected in early August 2020 after a short hypoxic period (6 days). Otherwise, summer anoxia ranged from 42 to 58 days (2023; 2022). Bottom-water was re-oxygenated in 1 to 11 hours, simultaneously with the previously described breakdown of thermal stratification in September. Anoxic conditions were reached again between November and December (earliest: winter 2019–2020; latest: winter 2022–2023). Winter anoxia lasted 153–198 days, with the shortest period occurring in winter 2022–2023, and the longest in 2019–2020. Re-oxygenation (4–32 hours) coincided with the breakdown of inverse stratification in May (timing previously described). Bottom-water pH ranged from moderately acidic to near neutral (5.68–7.28; median: 6.52; IQR: 6.25–6.80) largely showing a similar trend with DO conditions, increasing with rapid oxygenation. In contrast, pH also increased during persistent anoxia. The minimum pH values preceded the onset of anoxic conditions.

Turbidity ranged from 0.2 to 231.4 FNU, with a mean of 2.8 FNU. Across the sampling periods, mean values for summer, winter, and spring ranged from 1.71–4.38 FNU (2019; 2020), 2.41–3.89 FNU (2021–2022; 2022–2023), and 1.05–2.80 FNU (2021 and 2023; 2020), respectively. Median turbidity for the study period was 1.88 FNU (IQR: 0.21–3.55 FNU) despite the extreme peak detected between June and July in 2020 (within spring 2020 sampling period). An overall downward trend was observed within winter and spring periods, contrasting with the shared trend of SpCond, salinity, and TDS (see Figure 16). SpCond (mean: 55.1 µS/cm; range: 15.6–174.0 µS/cm), salinity (mean: 0.02 psu; range: 0.01–0.08 psu), and TDS (mean: 35.8 mg/l; range: 10.0–113.0 mg/l) increased synchronously during stable periods (i.e. persisting stratification in summer and winter) and decreased in association with rapid changes in bottom-water conditions (compare, for example, with the peaks in DO, depth, and discharge in Figure 16). A seasonal trend was also visible across sampling periods. Mean values were the lowest in summer, followed by winter, and the highest in spring. However, the maximum and minimum values were measured within the spring period. Interannually, the lowest mean values occurred in summer 2020, winter 2022–2023, and spring 2022 (SpCond: 31.1 µS/cm, 46.8 µS/cm, 68.7 µS/cm; TDS: 20.2 mg/l, 30.5 mg/l, 44.7 mg/l) and the highest in summer 2022, winter 2019–2020, and spring 2021 (SpCond: 36.6 µS/cm, 65.2 µS/cm, 74.2 µS/cm; TDS: 23.8 mg/l, 42.4 mg/l, 48.2 mg/l). Mean values for salinity were 0.01 psu (summer), 0.03 (winter; except 0.02 psu in winter 2022–2023), and 0.03 (spring).

The mean depth at the basin was 34.0 m (measured 1 m above the lake bottom). Depth ranged from 33.1 to 37.7 m, decreasing in winter and peaking during the spring flood. Seasonal pattern and the correspondence with discharge data is clearly visible in Figure 16. The mean discharge for the study period was 19.1 m^3/s ($n = 1545$). The range of mean discharges for each sampling period was as follows: summer, 13.0–27.9m^3/s (2021; 2022); winter, 6.8–8.7 m^3/s (2019–2020 and 2021–2022; 2022–2023); and spring, 24.7–53.1 m^3/s (2021; 2020). The lowest daily discharges occurred within the late winter and early spring sampling periods, between mid-February and mid-April. The highest daily discharges were recorded in spring, between mid-May and early June. In more detail, the lowest daily discharges were recorded in summer 2021 (8.6 m^3/s), winter 2021–2022 (3.4 m^3/s), and spring 2022 (3.3 m^3/s), whereas peaks for these sampling periods occurred in 2022 (48.2 m^3/s), 2020–2021 (26.1 m^3/s), and 2020 (357.6 m^3/s), respectively. Note that the June and July discharges in 2020 were included in spring sampling period and therefore do not show in the summer 2020 values. For example, the highest daily discharge for all summer months was recorded on 9 July 2020 (85.6 m^3/s). Daily discharges can be observed in Figure 16.

Ice cover period, from ice-on to ice-off, was recorded within the winter and spring sampling periods (see Appendix 7). The earliest ice-on was on 20 October (2021) and the latest on 21 November (2020), which was the only studied winter, when the formation of the continuous ice cover was not the first reported ice-on. Open water conditions were reached earliest on 21 May (2023) and latest on 3 June (2019). Ice cover period lasted from 189 to 225 days, in winter 2020–2021 and winter 2019–2020, respectively.

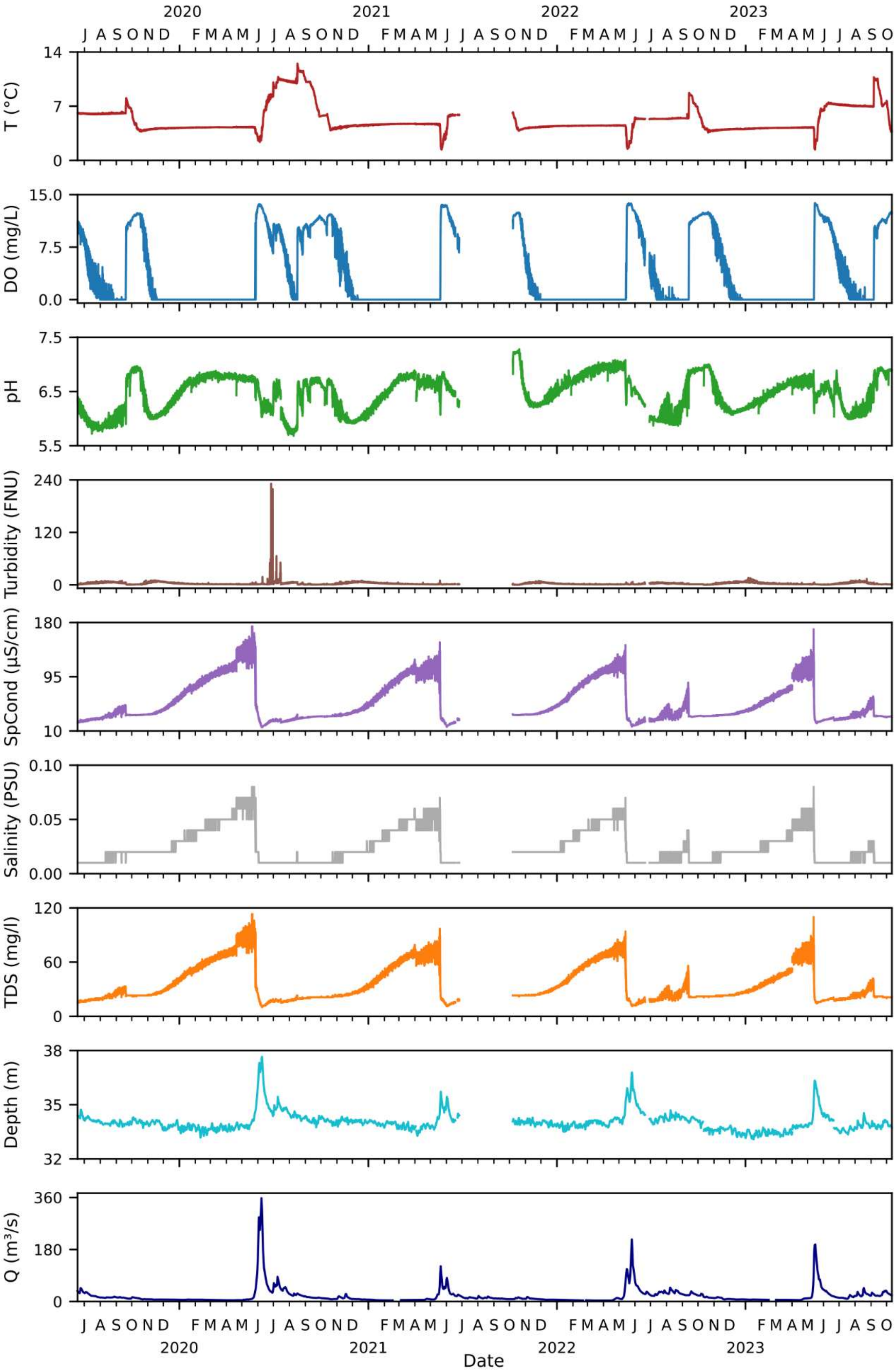

Figure 16. Hydrological data covering the study period. From top to bottom: hourly monitored water temperature (red), dissolved oxygen (blue), pH (green), turbidity (brown), specific conductance (purple), salinity (grey), total dissolved solids (orange), depth (turquoise), and daily discharge (dark blue) from Patoniva station obtained from Hertta database (Syke, 2024) at the bottom.

4.7 Meteorological conditions

Daily mean air temperatures, precipitation sums, and snow depths from June 2020 to October 2023 are presented in Figure 17. During the study period, the coldest month varied annually. February 2021 was the coldest (-15.6 °C) based on the monthly mean temperatures. Expect for August 2023, July was the warmest month of the year, with 2022 (15.4 °C) being the warmest. Precipitation was at its lowest in June 2023 (7.5 mm) and its highest in July 2020 (116.7 mm).

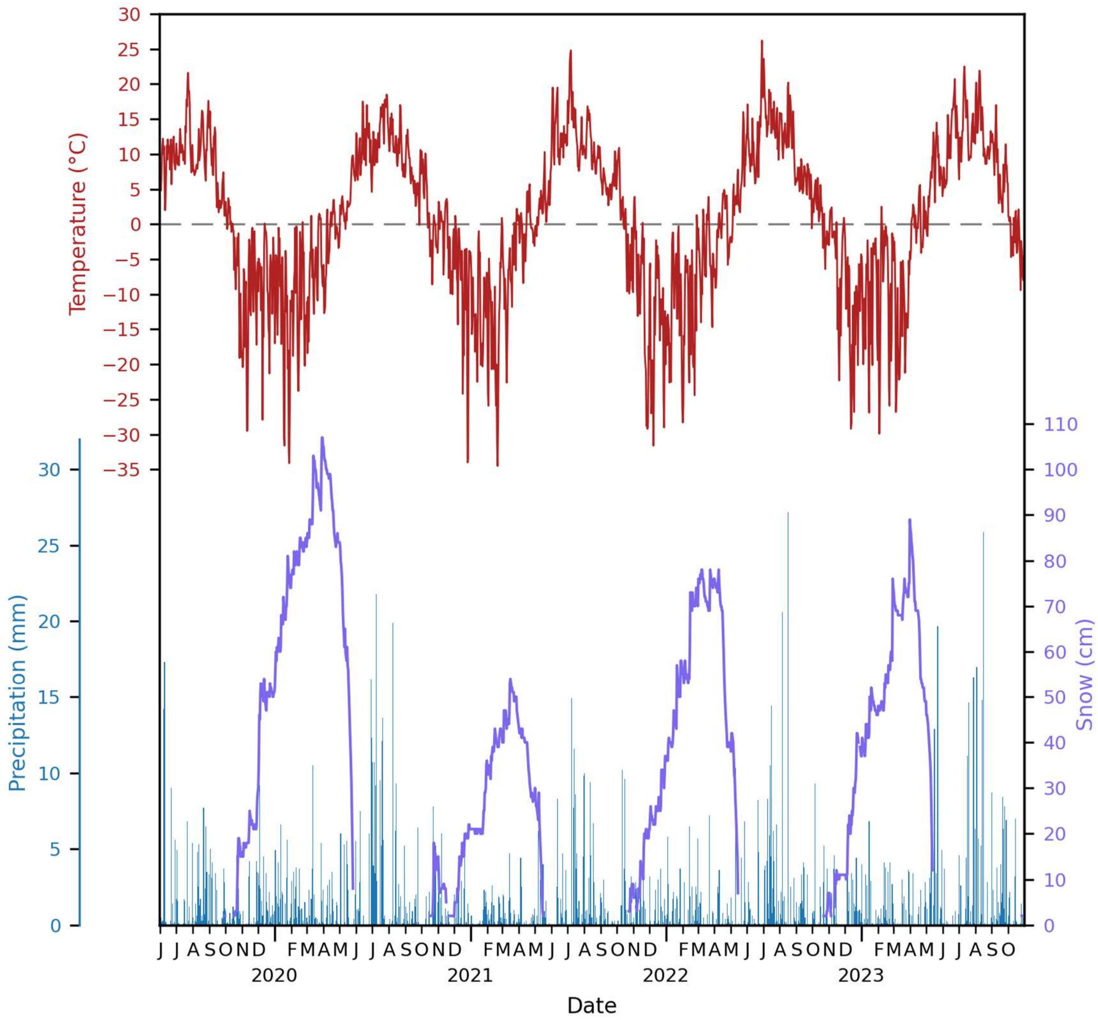

Figure 17. Daily mean air temperature (red), precipitation sum (blue) and snow depth (purple) from June 2020 to October 2023. Visualized based on the data obtained from FMI (2024a).

All sediment traps representing winter periods were set before the first ground-covering snow (2 cm). Expect for the first studied winter, the formation of the continuous snow cover fluctuated from a week to a month of ground-covering snow before the final, persisting snow cover, from which the count for consecutive snow cover days began (Figure 17). The earliest onset occurred in October (2019) and the latest in December

(2020). Snow persisted until mid-to-late May, ranging from 167 (winter 2020–2021) to 224 days (winter 19-20) in duration. Snowmelt was recorded in spring samples. Snow depth reached its maximum between March and April. The highest (107 m) and the lowest (54 m) maximum snow depths coincided with the longest and the shortest snow cover periods, respectively. Snow cover periods are summarized in Appendix 7.

Mean air temperatures calculated from daily means and precipitation sums are given here also for sampling periods (Table 3), as they varied in days and were not distributed evenly between months. Prolonged spring 2020 sampling period, and consequently short summer 2020 period are reported separately from other sampling periods. In a year-to-year comparison, summer 2022 (11.2 °C), winter 2020–2021 (-7.5 °C), and spring 2022 (4.5 °C) had the highest mean air temperatures. Conversely, mean air temperatures were the lowest in summer 2019 (10.3 °C), winters 2021–2022 and 2022–2023 (-8.6 °C), and spring 2023 (3.5 °C). Precipitation sums ranged from 107.7 to 227.5 mm, 115.7 to 200.1 mm, and 50.6 to 90 mm, for summer, winter and spring sampling periods, respectively. Precipitation sums were the lowest in summer 2019 (107.7 mm), winter 2020–2021 (115.7 mm), and spring 2021 (50.6 mm), while the highest sums were in summer 2023 (227.5 mm), winter 2019–2020 (200.1 mm), and spring 2023 (90 mm). The mean air temperature and precipitation sum were 7.5 °C and 218.9 mm for spring 2020, and 8.8 °C and 73.7 mm for summer 2020.

Table 3. Mean air temperatures and precipitation sums for all basin sampling periods (FMI, 2024a).

Sampling period	Mean air temperature (°C)	Precipitation sum (mm)
Summer 2019	10.3	107.7
Winter 2019–2020	-8.5	200.1
Spring 2020*	7.5	218.5
Summer 2020**	8.8	73.7
Winter 2020–2021	-7.5	115.7
Spring 2021	4.0	50.6
Summer 2021	10.7	144.1
Winter 2021–2022	-8.6	158.9
Spring 2022	4.5	56.9
Summer 2022	11.2	184
Winter 2022–2023	-8.6	129.5
Spring 2023	3.5	90.0
Summer 2023	11.1	227.5

Sediment sampling period longer * or shorter ** than intended

5 Discussion

5.1 Seasonality as a driver of sediment accumulation in Lake Kevojärvi

Lake Kevojärvi is a dimictic lake representative of subarctic regions (MacIntyre & Hamilton, 2024). As such, overturn occurred twice a year, oxygenating the bottom waters in spring and autumn, followed by thermal stratification of the water column. However, in contrast to stable inverse stratification beneath ice cover in winter, persistent stratification was detected in only four of the five studied summers; thermal stratification was strongly influenced by the summer conditions. The intermittently dimictic type of the lake in association with calm ice-cover period and intense snowmelt floods are considered as key factors enabling continuous varve formation (Ojala *et al*., 2013). In this study, the pronounced seasonal differences, combined with occasional interannual events, are suggested as key drivers of sedimentation in Lake Kevojärvi.

Sediment accumulation rates were the highest at both sites in spring, accounting for the majority of annual sedimentation in Lake Kevojärvi. Snowmelt is widely recognized as causing spring floods, which are extreme erosional events in boreal environments, resulting in the transport of significant volumes of sediments into a lake over a short time frame (Snowball *et al*., 1999; Ojala *et al.*, 2013; Johansson *et al*., 2019). The increased sediment load during snowmelt floods is also evidenced by greater varve thickness corresponding to the maximum annual discharge (Sander *et al.*, 2002). For example, Haltia *et al*. (2021) reported that the annual maximum discharges were associated with detrital snowmelt layers recognized in the varve sequence of Lake Kevojärvi. In the present study, spring samples were visibly coarser than those of summer and winter, reflecting the magnitude of sediment transport during snowmelt discharge peaks (Ojala *et al.*, 2013). In the Utsjoki River (2019–2023), maximum annual discharge occurred between mid-May and early June, around Lake Kevojärvi's ice-off and the peak of the spring flood. Stratified layers were mixed, and the hypolimnion became oxygenated.

After ice-off induced spring overturn, the surface of the isothermal water column warms as air temperatures rise in summer resulting in thermal stratification (Edmundson & Mazumder, 2002; MacIntyre & Hamilton, 2024). Previous studies considering climate warming and lake mixing regime have shown that warm summer temperatures prolong and reinforce the summer stratification through earlier onset and later overturn (Magee &

Wu, 2017; Mammarella *et al*., 2018; Woolway *et al*., 2021; Lincoln *et al*., 2025). In Lake Kevojärvi, stratification persisted from the onset in May-June until the overturn in September during the summers with distinct stratification. Stratifying water column was followed by gradually declining dissolved oxygen (DO) levels, and in stable conditions, hypolimnion became depleted in DO approximately one month after the onset of thermal stratification. In addition, a continuous period of fully anoxic (<0.5mg/l) bottom waters occurred in summer from August until the overturn in September. However, in summer 2020, the anoxic period persisted only 5 days prior to the early overturn in mid-August. Decomposition of organic matter in sediments consumes oxygen (Steinsberger *et al.*, 2020), and due to the inhibited vertical mixing during stratification, this may lead to oxygen depletion in the hypolimnion (Lincoln *et al.*, 2025). It is suggested that prolonged, stable stratification promotes DO depleted hypolimnion due to suppressed vertical mixing in water column (Jane *et al.*, 2023; Jansen *et al.*, 2024). Maximum discharges observed in summer were lower than in spring. However, mean discharges representing the summer sampling periods were occasionally comparable to those of spring sampling periods. Nevertheless, sediment accumulation remained lower in summer, underlining the importance of snowmelt floods for annual sediment deposition.

In winter, sediment accumulation was minimal, and mean discharge was at its annual minimum. The observed fine-grained homogenous sediments suggest low-energy depositional conditions (Tiljander *et al.*, 2003; Ojala *et al.*, 2013). Winter accumulation was most likely dominated by the deposition following the seasonal peak discharges measured in October-November, after which discharge began to decline, reaching annual minima between February and April. Sediment transport from the catchment is also inhibited by the ground frost (Johansson *et al*., 2019) and snow cover (Saarni *et al.*, 2021). In addition, Lake Kevojärvi was covered by ice from ice-on in October-November to ice-off in May-June (6–7 months). Even a shorter period of annual ice cover is shown to result in slow sediment accumulation (Tylmann *et al.*, 2012; Ojala *et al.*, 2013). According to Itkonen and Salonen (1994), ice cover prevents wave action and, therefore, the resuspension of sediments from the littoral zone. Without mixing, the conditions under ice are calm and inverse stratification is formed (Lincoln *et al.*, 2025) leaving the bottom waters depleted in DO until the overturn in spring. In Lake Kevojärvi, bottom waters remained anoxic for 5–6 months, from November-December. Moreover, negligible light penetration through ice and snow, together with cold, nutrient-poor waters, suppresses organic production, further reducing winter accumulation rates (Ojala *et al.*, 2013).

Although the seasonal pattern of accumulation rates was consistent, magnitudes and the sediment composition varied between the sites and within seasons. At the delta, the dominance of spring accumulation was more pronounced, with higher rates than at the basin, whereas summer and winter rates at the basin exceeded those at the delta. These observations are explained by the defining characteristics of basin and delta as depositional environments. Delta is a principal entrance of minerogenic matter into a lake (Cohen, 2003), which primarily records fluvial deposition (Vonk *et al.*, 2016) characterized by allochthonous materials (Håkanson & Jansson, 2002). The vicinity of the river-mouth enhances the role of discharge as a key factor in sediment deposition (Håkanson & Jansson, 2002). These conditions favour the deposition of heavier (and coarser), often minerogenic, particles (Håkanson, 2007) whereas lighter material is transported further into the lake (Håkanson & Jansson, 2002). Fine-grained matter requires low-energy environment to accumulate (Håkanson, 2007), such as deep basin. There sediments can settle without resuspension by, for example, waves or bottom currents. The deep lake basin is often characterized by continuous sedimentation (Ojala *et al.*, 2013), as evidenced by continuously preserved varves in the western basin of Lake Kevojärvi (Haltia *et al.*, 2021). Finally, it must be noted that especially during the intense spring floods, the high discharge at the river mouth may have altered the upright position of the collector tubes at the delta. This in turn may have disrupted sediment sampling.

5.2 Hydroclimatic controls on sediment composition

Lithogenic particles, biogenic silica, organic matter, and carbonates together with other authigenic minerals represent the four main components of lake sediments according to Bertrand *et al.* (2024). In lake Kevojärvi, sediment composition was more minerogenic than organic at both sites throughout all seasons, but basin sediments had generally higher OM content compared to the delta. Delta sediment composition was variable, with OM content appearing relatively lower in spring. This does not, however, indicate decreased organic accumulation during spring floods, as organic flux peaked alongside minerogenic flux at both sites. Instead, OM content decreased due to the dilution by minerogenic input during the spring floods at the delta. Additionally, macroscopic terrestrial plant remains were abundant in all spring samples at both study sites, suggesting increased OM transport from the catchment (Ojala *et al*., 2013) during the spring floods. Otherwise, seasonal patterns in OM content were not detected, as shown in Figure 6 and 7. Primary production in the lake during the growing season could have been reflected in elevated OM content in summer samples (Ojala *et al*. 2013). This seasonal signal may have been diminished due to the discussed terrestrial OM input in spring. In addition, the slow settling of the fine-grained OM may have maintained the overall OM content in sediments also in winter, while minerogenic matter remained trapped within the catchment by snow cover (Saarni *et al*., 2021) and ground frost (Johansson *et al*., 2019).

Sediment geochemistry serves as an indicator of the described sediment components due to the elements associated with them (Bertrand *et al.*, 2024). However, elements can overlap between the groups. For example, the elements considered in this study can be divided into these four groups as follows: Ti, Al, K, Ca, Fe, Si are prevalent in lithogenic particles, Si can also be of biogenic origin (e.g., diatom frustules), P is present in organic matter, and Ca is a building block in carbonates (Bertrand *et al.*, 2024). In addition, redox-sensitive elements (Mn, Fe, P, and S) can be of authigenic origin (Håkanson & Jansson, 2002). All these elements are rock-forming (Rothwell & Croudace, 2015), but the geochemically stable Ti, Al, and K, occur only in lithogenic fraction (Bertrand *et al.*, 2024) reflecting catchment erosion and transport of detrital minerogenic matter into the lake (Ojala & Alenius, 2005). It should be noted that minimal amounts of material and not pulverised subsamples (i.e., gently homogenized due to their reuse in another study) used in μ-XRF analysis, but also the small number of samples in PCA, although exceeding the number of variables (9), limit the reliability of the geochemical results.

The observed decrease in Si/Al, Si/Ti, and Si/K ratios in spring, point to the dominance of allochthonous lithogenic sedimentation rather than autochthonous biogenic siliceous production in Lake Kevojärvi (Rothwell & Croudace, 2015; Bertrand *et al.*, 2024). In accordance with the maximum discharges, the elevated Ti/Al ratio at the basin in spring indicates a change in transportation energy enabling coarse-grained/heavy mineral particles to be transported further from the river mouth (Bertrand *et al.*, 2012; Rothwell & Croudace, 2015). The coarser spring grain size can be observed in the elemental maps of samples winter 2021–2022, spring 2022, and summer 2022 from basin (Figure 8). At the delta, this seasonal grain-size related pattern was not detected. It may be overridden by the generally heterogenous and coarse-grained sediment composition characteristics to delta (Håkanson, 2007). This is in line with Bertrand *et al.* (2012) who observed Ti and Fe to be associated with coarse-grained and heavy minerals indicating changes in sediment transport energy, whereas the distribution of Al was not tied to depositional events. Despite the differences between the saline fjord system in Northern Chilean Patagonia represented in Bertrand *et al*. (2012) and the subarctic lacustrine environment of this study, the observed Ti/Al ratio suggests that the distribution of lithogenic elements in Lake Kevojärvi is due to the changes in transportation energy and recorded in the sediments deposited at the basin. In addition, the predominantly lower Ti/Al ratios at the basin were consistent with the detected downstream decrease of the Ti/Al ratio in Chen *et al.* (2013) revealing the diminishing transport energy from the delta to basin.

In line with the observed elemental ratios, the solely lithogenic fraction of elements is associated with spring, as is apparent in PCA biplots (Figure 13 and 14). The negative loadings of Ti, Al, and K align with the PC1 (Figure 13 and 14) dominated by Ti (-0.56) at the basin, and Ti (-0.50) and Al (-0.48) at the delta. In contrast, redox-sensitive elements were associated with winter and summer, and showed positive loadings on PC1, of which the most dominant was P (basin: 0.53; delta: 0.42). Supported by the detected seasonal patterns of SAR, sediment geochemistry suggests that detrital input is the main driver of seasonal sedimentation and sediment characteristics in lake Kevojärvi reflecting enhanced catchment erosion and detrital transport during spring floods in agreement with Lincoln *et al.* (2025). In their study, PC1 represented seasonal variations between allogenic detrital and authigenic organic sedimentation. The observed PC1 loadings of P in this study could indicate the accumulation of organic-bound P during winter and the growing season in summer. Nevertheless, this was inconsistent with the OM fluxes, which followed the total accumulation rates rather than summer and winter seasons. Due to the wide fractional distribution of P in lacustrine sediments (Håkanson & Jansson, 2002), PCA results can also indicate the deposition of fine-sized inorganic particles, as in Kaiserli *et al*. (2002). Additionally, primary production was not expected to be a major contributing factor due to the oligotrophic nature of the lake (Håkanson, 2007). Therefore, PC1 reflects the shifts in grain size representing seasonal variations in transport energy rather than shifts in OM and MM deposition in Lake Kevojärvi. Near zero loadings (PC1) show that Ca is not a contributing factor to detrital input to the lake (Bertrand *et al.*, 2024), which is consistent with the absence of carbonates in the catchment (GTK, 2022).

According to the PCA results from both sites, Fe and Mn were associated together, as well as S and P. However, redox-sensitive elements showed difference in PC2 between the sites. In contrast to PC1, Mn and Fe were negatively loaded, whereas P and S were again positive at the basin. Conversely, the opposite was observed for PC2 loadings at the delta. The major contributors were Mn (basin: -0.57; delta: 0.47), P (basin: 0.50; delta: -0.44), and S (basin:0.51; delta: -0.58) at both sites. Fe was moderately positive at the delta (0.38) and weakly negative at the basin (-0.17). The strong contribution of redox-sensitive elements and the poor representation of lithogenic fraction on PC2 may reflect the dominance of post-depositional processes as a secondary driver of the sediment geochemistry in Lake Kevojärvi (Lincoln *et al.*, 2025). However, the observed differences on PC2 indicate contrasting redox-controls on the mobility of Fe, Mn, P, and S between the sites. Hydrological monitoring was not conducted at the delta, but its proximity to the river mouth, water depth (~20 m), and the interpreted thermal stratification depths (Figure 15) suggest that delta is likely to remain oxygenated in summer in contrast to the DO conditions at the basin.

The increase of specific conductance, salinity, and TDS during the stratified periods (summer and winter) suggests progressive enrichment of dissolved solids in hypolimnion followed by rapid redistribution during seasonal overturn. According to (Coutelot *et al.*, 2025), prolonged anoxia during stratification indicates mobilization of redox-sensitive elements, such as Mn and Fe. The indicated reduction of Mn and Fe oxides is also supported by the observed increase of pH under prolonged hypolimnetic anoxia (Soetaert *et al.*, 2007). Owing to the lack of carbonates in the catchment, even peak pH values remained near neutral (Soetaert *et al.*, 2007). In Lake Kevojärvi, seasonal variations in redox-conditions were not recorded in Mn/Fe ratio, as it decreased in spring at the basin and did not show any seasonal trend at the delta. The use of the Mn/Fe ratio as a redox proxy is based on the stronger sensitivity of Mn to oxygen availability, and therefore elevated Mn/Fe ratios are expected when bottom waters are oxygenated (Makri *et al.*, 2021), for example, during the overturn in spring after the winter anoxia. However, here the detrital input to the lake distorts the visibility of redox variations in Mn/Fe (Makri *et al.*, 2021) repeating the same signal as observed in Ti/Al ratio (Bertrand *et al.*, 2012).

5.3 Interannual variability in seasonal sedimentation and hydroclimatic conditions

Interannual variability in seasonal sedimentation and hydroclimatic conditions was detected alongside the general seasonal cycles. However small sample sizes limited the interpretations for summer, but particularly for winter, when even the 0.5 g dry sample weight was not exceeded. For example, the observed elevated Ti/Al ratio (basin; see Figure 11) in winter 2021–2022 unlikely reflected enhanced accumulation of coarse-grained minerogenic matter during the period of the lowest measured mean discharge and sediment accumulation. Additionally, some of the finest material may have been lost in the early stages of sampling and sample preparation, potentially reducing the reliability of the results, particularly for small samples. The effect is more pronounced in interannual comparisons based on single samples than in seasonal pattern observations. In contrast, greater emphasis should be placed on interannual variability of seasonal organic and minerogenic content, rather than on intra-annual variability. LOI sample sizes were consistent interannually (except for delta samples summer 2020 and winter 2021–2022) but not across seasons, which impacts the sample-size dependent LOI (550 ºC; Heiri *et al.*, 2001). Nevertheless, also the interannual variations based on LOI should be interpreted with caution due to the small subsample sizes (see Appendix 2).

Shorter ice-cover periods in winter resulted in elevated sediment accumulation rates. The main transport events most likely occurred in the beginning of the winter sampling periods, during which the maximum discharges were observed, and ground frost, snow cover, and ice cover were still forming allowing sediment transport from the catchment. However, no significant interannual differences in sediment composition were detected, suggesting stable conditions during the ice-cover period, as can be seen in Figure 16 (Ojala *et al.*, 2013). Therefore, the predicted future changes in autumnal hydroclimatic conditions, for example, enhanced storminess (Lincoln *et al.*, 2025) and delayed ice-on (IPCC, 2022), are expected to increase winter sedimentation in Lake Kevojärvi. Greater summer rainfall was associated with elevated sediment accumulation rates at both sites but was not reflected in the discharge. In addition, summer 2021 differed from the observed pattern with the highest sediment accumulation rates at the basin. The lowest observed summer discharge and its geochemical position closest to the winter cluster in basin PCA biplot (Figure 13) could indicate accumulation of fine-grained material (Lincoln *et al.*, 2025). Despite the lack of DO data, anoxic conditions were expected based on the strong thermal stratification visible in Figure 15 (Jane *et al.*, 2023). Therefore, the peak in Mn/Fe ratio supports the deposition of fine-grained material (Bertrand *et al.*, 2012) rather than changes in redox-conditions. There was neither hydrological monitoring nor delta sample from summer 2021 due to the EXO2 sonde power failure and malfunction of the delta sediment trap. This undermined a detailed assessment of the possible causes behind the observed differences relative to other summers. Overemphasis should also be avoided with any single depositional events (Saarni *et al.*, 2017).

The most pronounced variation in hydrological conditions was observed between the summer periods. In summer 2020, the water column remained unstratified enabling oxygenation of the bottom waters (Jane *et al.*, 2023) with only a brief oxygen depleted period detected in August. Continuous mixing reduced the enrichment of dissolved solids in the hypolimnion (Coutelot *et al.*, 2025), as indicated by the relatively stable TDS and specific conductance (Figure 16). The several major turbidity peaks may indicate resuspension due to mixing, but their significance and occurrence during the only summer with oxygenated bottom waters most likely represents bioturbation (Zolitschka *et al.*, 2015). Further determination of bioturbation would require microfacies analysis of the varved sediments (i.e., core samples), which was outside the scope of this study. This was also the summer of the lowest OM percentage (Figure 6) and flux at the basin, but also the only occasion when the observed sediment organic content was lower relative to the delta. Oxygen availability throughout the summer may have enhanced the decomposition of the deposited OM, as it is better preserved under anoxic conditions (Steinsberger *et al.*, 2020). In addition, sediment geochemistry distinguished summer 2020 from the other years observed at the basin. In PCA biplot (Figure 13), it was clearly separated from the grouped summer samples, opposing the S and P vectors while aligning with the lithogenic fraction on PC1. It must be noted that summer 2020 samples represented only the latter part of the intended sampling period, potentially affecting the results. However, while summer 2020 was an outlier at the basin, the corresponding sample did not show a significant difference in geochemistry at the delta (Figure 14). Additionally, summer 2020 exhibited the highest sediment organic content among all seasons at the delta (Figure 7), which is typical of sediment deposited between late summer and autumn (Ojala *et al.*, 2013).

The mean air temperatures in summer 2020 were rather low, inhibiting the formation of thermal stratification (Figure 15). In turn, the largest surface-to-bottom temperature difference indicated that the strongest thermal stratification occurred during the warmest summer (2022). However, despite the lowest observed mean summer temperatures, the water column also became thermally stratified in 2019, albeit with a less distinct thermocline (Figure 15). The highest observed summer discharge peak following the heavy precipitation in July 2020 likely maintained vertical mixing (Lincoln *et al.*, 2025), as evidenced by the temporal correspondence with increased bottom-water DO levels (Figure 16). Unfortunately, the event cannot be distinguished in sediment accumulation rates due to its occurrence within the prolonged sampling period. However, the hydroclimatic conditions of the preceding spring may have contributed the most to the development and persistence of thermal stratification. A slowly progressing spring (i.e., delayed snowmelt and ice-off) following a snow-rich winter resulted in a late spring overturn (Figure 15) and significant flooding in 2020 (see water depth and discharge in Figure 16). Water column remained close to isothermal, with the highest measured discharge peak occurring after the typical onset of summer stratification. Therefore, the interannual differences in hydroclimatic conditions suggest that low summer temperatures promote vertical mixing and, in combination with pronounced snowmelt floods and delayed spring overturn, may prevent the formation of thermal stratification in Lake Kevojärvi. According to the observed summer thermal structures, Lake Kevojärvi's mixing regime is likely to become permanently dimictic under the warming summer temperatures.

Despite the prolonged sampling period, the intense inflow during the spring 2020 snowmelt flood was reflected in increased sediment accumulation (Ojala *et al.*, 2013). In addition, the basin sample (spring score) showed a strong association with the lithogenic fraction along PC1 (Figure 13). The elevated SAR was also recorded in delta winter 2019–2020 sample. However, elevated discharge was not linearly related to interannual variations in seasonal sediment accumulation rates. In 2022, discharge was elevated, although it was not significantly different from 2023. The timing of snowmelt, ice-off, and spring overturn was also similar between the years. The local snow water equivalents were not available from the area. Therefore, the water content in snow, likely contributing to snowmelt-induced sediment transport (Ojala *et al.*, 2013; Saarni *et al.*, 2017), was not examined in further detail. Nevertheless, SAR in spring 2022 was significantly high, particularly at the delta. The reduced snowpack in winter 2020–2021 and the resulting low-energy transport in spring 2021 may have contributed to the elevated SAR as a delayed transport from the catchment sediment storages in spring 2022 (Slaymaker *et al.*, 2003). More importantly, the major discharge peak in spring 2022 was preceded by a discharge peak of nearly the same magnitude as in 2021. The double-peaking flood event most likely caused the observed increase in accumulation rates, as previously reported by Blåfield *et al.* (2025) for a subarctic river northeast from Lake Kevojärvi. They suggest that multi-peak events in subarctic areas are becoming more frequent instead of single snowmelt-flood events, leading to elevated sediment transport in the warming future. The spring 2022 samples were also characterized by a muddy odour and brownish excess water, in contrast to the odourless, greyish water observed in the other samples. In addition, the highest sediment organic content and flux occurred at the basin in spring 2022, which may indicate enhanced erosion and transport from an organic-rich catchment store such as peatlands (Mattsson *et al*., 2005). However, sediment geochemistry was consistent with springs 2021 and 2023.

5.4 Future perspectives

Seasonal sample sizes affected the availability of material for the analyses. This was more problematic with delta samples due to the minimal sediment accumulation in summer and winter. In addition, elevated discharge in the vicinity of river mouth complicated consistent sample collection from the delta, especially during the spring floods. Therefore, the observations in this study support the previous decision to discontinue sediment trap monitoring at the delta in 2024. Instead, efforts should be focused on the continuous monitoring of sedimentation at the basin. To avoid disruptions in the sampling, it was shown that the minimum of two collector tubes is crucial. However, additional collector tubes would ensure successful sampling and benefit material sufficiency. Error limits and accuracy of sample collection was not evaluated in this study. This would be easily achieved by emptying the two, or additional collector tubes in individual buckets instead of a single bucket and then comparing the accumulated sediments, as in Ojala *et al.* (2013). It is noteworthy that their results supported the sediment trap method also employed in this study.

Sampling three times a year was suitable for detecting seasonality but also interannual variability in sedimentation, provided that the sampling periods were kept consistent.

Subsamples for diatom analyses were taken from the samples of this study. If this is continued in the future, more frequent sampling should be considered (Ojala *et al.*, 2013) and the required dry subsample size (now ~100 mg was targeted) should be assessed to improve sample sufficiency for other analyses. The sample plate made for the μ-XRF subsamples in this study worked well and enabled their reuse in diatom analysis. Due to the reuse, dried sediments were not finely powdered. The amount of reused material per subsample was minimal (15–76 mg). Therefore, the need for reuse should be reconsidered depending on the initial sample sizes. Alternatively, powdered subsamples could be utilized in other analyses, for example, in LOI measurements. Heiri *et al*. (2001) suggest usage of samples approximately the same weight for LOI at 550 ºC. Same intra-annual subsample sizes for LOI could not be reached due to the seasonal variability and dominance of spring in SAR. Therefore, season-specific sample sizes were used. In addition, the use of 1 g of dry sediment for LOI was reported in Bertrand *et al.* (2024). LOI is a destructive method, and therefore even the spring subsamples were kept at 0.5 g. However, a specific sample size was not determined in the methodology of Heiri *et al*. (2001) that was the basis for LOI measurements in this study. Instead, they highlighted the importance of reporting sample sizes, exposure time, and furnace conditions, which were followed in this study.

According to Bertrand *et al.* (2024), measuring total organic carbon (TOC) is suggested to enable intra-annually consistent sample sizes (~0.05 g), improve the accuracy in determining sediment OM content, and enhance result comparability in future studies. Most importantly, TOC measurements would provide insight into carbon burial in subarctic Lake Kevojärvi, contributing to a better understanding of already recognized role of lakes in global carbon cycle (Tranvik *et al.*, 2009) from the region experiencing the fastest rate of climate change (Rantanen *et al.*, 2022). C/N measurements should be considered to trace the origin (i.e., autochthonous, or allochthonous) of the deposited OM in Lake Kevojärvi, as in Tiljander *et al*. (2006). This would particularly profit in understanding sediment sources in summer and their interannual variability. Additionally, detailed analysis of P-fractions would enable the interpretations of P behaviour in variating redox-conditions, i.e., its proneness to be released back to the nutrient cycle from the sediment (Kaiserli *et al*., 2002).

Not only the accumulation of OM contributes to the sedimentation during the growing season, but also the complex hydroclimatic conditions due to the open-water period. Wind (speed and direction) has been recognized to contribute to sediment accumulation during the open-water period in lakes (Zolitschka *et al.*, 2015; Johansson *et al.*, 2019). In addition, it promotes mixing and therefore may alter lake thermal structure (Lincoln *et al.*, 2025) occasionally exceeding the effect of air temperature variations, as in Magee and Wu (2017). In the oligotrophic Lake Kevojärvi, organic matter is not the only major driver of sedimentation during the growing season. During the open-water period, multiple factors may contribute to the rate and composition of the accumulated sediments in late spring and summer. For example, the exact causes of the elevated SAR in summer 2021 were not identified in this study. Integrating wind observations into the sedimentation study conducted in Lake Kevojärvi would enhance understanding of both the observed differences in summer stratification and the unexplained variations in sediment accumulation rates during the summer period. Wind speed and direction are available from Kevo station, from which all the meteorological data used in this study were obtained.

Seasonal differences in grain size and heterogeneity were roughly distinguishable with the naked eye and in the elemental maps. However, grain-size analysis is strongly suggested, particularly the use of laser diffractometer over the traditional settling methods to minimize the required subsample volume. Grain size is crucial for determining interannual variability in seasonal sedimentation (Ojala *et al.*, 2013). It would also support the interpretations made based on the sediment geochemistry, for example, the increase of Ti and Fe detected at the basin during the expected deposition of coarse-grained material. Moreover, the small number of samples per season (three at lowest) increased the sensitivity to outliers, which was particularly problematic for PCA. To move from simple descriptions of the data to reliable interpretations and comparability, more samples are needed. This will be naturally enhanced in summer 2026, after which sediment-trap sampling has been conducted for ten consecutive years at the basin in Lake Kevojärvi. In addition to the utilization of the samples taken prior to and following the study period (2019–2023), the modern sedimentation in relation to the hydroclimatic conditions documented in this study should be compared with the past sedimentation recorded in the annually laminated sediments in the basin, as in Ojala *et al.* (2013). Furthermore, it is strongly advised to continue sediment trap and hydrological monitoring in Lake Kevojärvi, as even within this study period, potential responses to the climate change emerged, such as double-peaking flood events in spring and strengthening thermal stratification under warm summer air temperatures.

6 Conclusions

Near-bottom sediment-trap sampling and hydroclimatic observations were combined in this thesis project to study seasonal sedimentation and sediment characteristics in Lake Kevojärvi. Two depositional environments were studied, revealing a decrease in transport energy from the river mouth toward the lake basin. Delta represented a high-energy depositional environment defined by predominantly discharge-driven, minerogenic-rich sediment accumulation. Basin was characterized by continuous sedimentation allowing seasonal observations at an interannual timescale.

Annual sedimentation was dominated by snowmelt-driven spring floods, while minimal accumulation occurred under ice-cover in winter, as was expected for a subarctic lake. In addition to the sediment accumulation rates, seasonality was recorded in sediment geochemistry. Spring sedimentation (lithogenic fraction) was distinguished from summer and winter (redox-sensitive elements) based on PCA and elemental ratios. Detrital input (PC1) was the primary control on seasonal sedimentation, likely reflecting changes in transport energy, particularly in the basin. Secondary driver (PC2) represented post-depositional processes in association with redox conditions. Mn/Fe ratio was controlled by grain-size changes, similarly to Ti/Al ratio, and did not reflect redox conditions.

Persistent stratification during winter (inverse) and summer (thermal) led to gradual enrichment of dissolved solids and decrease in dissolved oxygen resulting in hypolimnetic anoxia. The overturn occurred twice a year, suggesting a dimictic mixing regime. Under these conditions, delta was expected to remain oxygenated throughout the summer. However, an intense snowmelt flood followed by cool summer temperatures sustained vertical mixing in summer also at the basin. With the increasing summer temperatures, the lake may be transitioning from an occasionally monomictic system towards a more consistently dimictic mixing regime in the future.

Overall, this study demonstrates the major hydroclimatic controls on seasonal sedimentation in Lake Kevojärvi. These present-day findings can be used to complement the reconstructions of the past hydroclimatic conditions derived from the annually laminated sediments present in the lake's basin. Moreover, continuation of the ongoing sediment trapping and hydrological monitoring remains essential for recording lake's responses to the future climate forcing. Future work incorporating grain-size analyses and organic matter characterization (e.g., C/N, TOC, P-fractions) would further refine interpretations of sediment sources and transport processes.

7 Acknowledgements

I would like to express my gratitude to my supervisor, Associate Professor Saija Saarni, for her guidance and encouragement throughout my thesis journey. I am especially thankful for the opportunities she provided beyond the scope of the thesis work. My heartfelt thanks also go to Maarit Kalliokoski for conducting the μ-XRF measurements and for familiarizing me with the details of the technique through her work. I am also grateful to the staff at Kevo Research Station, without whom this thesis would not have been possible. Additionally, I would like to acknowledge the SENCE research group and the staff at Geohouse for their contributions. A special thank you to my friend Julia Puustinen for her collaboration during the early stages of our theses. Finally, I extend my warmest thanks to my friends and family, both near and far, for their unwavering support and patience throughout this entire process. Kiitos!

References

Benson, B.J., Magnuson, J.J., Jensen, O.P., Card, V.M., Hodgkins, G., Korhonen, J., Livingstone, D.M., Stewart, K.M., Weyhenmeyer, G.A. and Granin, N.G. (2012). Extreme events, trends, and variability in Northern Hemisphere lake-ice phenology (1855–2005). *Climatic Change* 112(2), pp. 299–323. doi:10.1007/s10584-011-0212-8.

Bertrand, S., Hughen, K.A., Sepúlveda, J. and Pantoja, S. (2012). Geochemistry of surface sediments from the fjords of Northern Chilean Patagonia (44–47°S): Spatial variability and implications for paleoclimate reconstructions. *Geochimica et Cosmochimica Acta* 76, pp. 125–146. doi:10.1016/j.gca.2011.10.028.

Bertrand, S., Tjallingii, R., Kylander, M.E., Wilhelm, B., Roberts, S.J., Arnaud, F., Brown, E. and Bindler, R. (2024). Inorganic geochemistry of lake sediments: A review of analytical techniques and guidelines for data interpretation, *Earth-Science Reviews* 249, p. 104639. doi:10.1016/j.earscirev.2023.104639.

Birks, H.H. and Birks, H.J.B. (2006). Multi-proxy studies in palaeolimnology, *Vegetation History and Archaeobotany*. 15(4), pp. 235–251. doi:10.1007/s00334-006-0066-6.

Blåfield, L., Gonzales-Inca, C., Alho, P. and Kasvi, E. (2025). Morphological response to climate-induced flood event variability in a sub-arctic river. *Earth surface dynamics* 13(5), pp. 827–844. doi:10.5194/egusphere-2024-3802.

Bloesch, J. and Burns, N.M. (1980). A critical review of sedimentation trap technique. *Schweizerische Zeitschrift für Hydrologie* 42(1), pp. 15–55. doi:10.1007/BF02502505.

Bonk, A., Tylmann, W., Amann, B., Enters, D. and Grosjean, M. (2015). Modern limnology and varve-formation processes in Lake Żabińskie, northeastern Poland: comprehensive process studies as a key to understand the sediment record. *Journal of Limnology* 74(2). doi:10.4081/jlimnol.2014.1117.

Brouwer, P. (2010). *Theory of XRF*. 3rd edn. Almelo: PANalytical B.V. p. 59.

Chen, H.-F., Yeh, P.-Y., Song, S.-R., Hsu, S.-C., Yang, T.-N., Wang, Y., Chi, Z., Lee, T.-Q., Chen, M.-T., Cheng, C.-L., Zou, J. and Chang, Y.-P. (2013). The Ti/Al molar ratio as a new proxy for tracing sediment transportation processes and its application in aeolian events and sea level change in East Asia. *Journal of Asian Earth Sciences* 73, pp. 31–38. doi:10.1016/j.jseaes.2013.04.017.

Cohen, A.S. (2003). *Paleolimnology: The History and Evolution of Lake Systems*. 1st edn. Oxford: Oxford University Press. p. 500.

Coutelot, F., Kaplan, D.I., Kersting, A.B., Zavarin, M. and Powell, B.A. (2025). Effect of seasonal anoxia on geochemical cycling in a stratified pond: Comparison to cooler pond conditions 40 years ago. *Science of The Total Environment* 976, p. 179337. doi:10.1016/j.scitotenv.2025.179337.

Dean, W.E. (1974). Determination of carbonate and organic matter in calcareous sediments and sedimentary rocks by loss on ignition; comparison with other methods. *Journal of Sedimentary Research* 44(1), pp. 242–248. doi:10.1306/74D729D2-2B21-11D7-8648000102C1865D.

Dickman, M. (1985). Seasonal succession and microlamina formation in a meromictic lake displaying varved sediments. *Sedimentology* 32(1), pp. 109–118. doi:10.1111/j.1365-3091.1985.tb00495.x.

Edmundson, J.A. and Mazumder, A. (2002). Regional and hierarchical perspectives of thermal regimes in subarctic, Alaskan lakes. *Freshwater Biology* 47(1), pp. 1–17. doi:10.1046/j.1365-2427.2002.00775.x.

Flude, S., Haschke, M. and Storey, M. (2017). Application of benchtop micro-XRF to geological materials. *Mineralogical Magazine* 81(4), pp. 923–948. doi:10.1180/minmag.2016.080.150.

FMI (2024a). *Havaintojen lataus, Säähavainnot*. Finnish Meteorological Institute. <https://www.ilmatieteenlaitos.fi/havaintojen-lataus> (Accessed: 15 March 2024)

FMI (2024b). *Ilmatieteen laitoksen havaintoasemat*. Finnish Meteorological Institute. <https://www.ilmatieteenlaitos.fi/havaintoasemat> (Accessed: 25 October 2024)

FMI (2024c). *Lämpimin ja kylmin paikka vuosittain*, Finnish Meteorological Institute. <https://www.ilmatieteenlaitos.fi/lampimin-ja-kylmin-paikka-vuosittain> (Accessed: 25 October 2024).

FMI (2024d). *Temperature and precipitation statistics from 1961 onwards*, Finnish Meteorological Institute. <https://en.ilmatieteenlaitos.fi/statistics-from-1961-onwards> (Accessed: 20 October 2024).

GTK (2010). *Superficial deposits of Finland 1:200 000 (sediment polygons)*, Geological Survey of Finland. <https://hakku.gtk.fi/en/locations?id=3> (Accessed: 25 October 2024).

GTK (2021). *Glacial features*, Geological Survey of Finland. <https://hakku.gtk.fi/en/locations?id=186> (Accessed: 25 October 2024).

GTK (2022). *Bedrock of Finland 1:200 000*, Geological Survey of Finland. <https://hakku.gtk.fi/en/locations?id=2> (Accessed: 25 October 2024).

Haltia, E., Leppänen, A.-P., Kallio, A. and Saarinen, T. (2021). Sediment profile dating and reconstructing nuclear events from annually laminated lake sediments in northern Finland. *Journal of Environmental Radioactivity* 233, p. 106611. doi:10.1016/j.jenvrad.2021.106611.

Hammer, Ø., Harper, D.A.T. and Ryan, P.D. (2001). PAST: Paleontological Statistics software package for education and data analysis. *Palaeontologia Electronica* 4(1), 9 pp.

Hargrave, B.T. and Burns, N.M. (1979) Assessment of sediment trap collection efficiency. *Limnology and Oceanography* 24(6), pp. 1124–1136. doi:10.4319/lo.1979.24.6.1124.

Haschke, M. (2014). *Laboratory Micro-X-Ray Fluorescence Spectroscopy: Instrumentation and Applications*. Cham: Springer International Publishing (Springer Series in Surface Sciences). doi:10.1007/978-3-319-04864-2.

Heiri, O., Lotter, A.F. and Lemcke, G. (2001). Loss on ignition as a method for estimating organic and carbonate content in sediments: reproducibility and comparability of results. *Journal of Paleolimnology*, 25(1) pp. 101–110. doi:10.1023/A:1008119611481.

Håkanson, L. (2007). Lake Environments, in Perry, C. and Taylor, K. (eds) *Environmental Sedimentology*. Oxford: Wiley-Blackwell, pp. 109–143.

Håkanson, L. and Jansson, M. (2002). *Principles of lake sedimentology*. Reprint of 1st ed. Caldwell, N.J: Blackburn Press.

IPCC (2021). *Climate Change 2021 – The Physical Science Basis: Working Group I Contribution to the Sixth Assessment Report of the Intergovernmental Panel on Climate Change*. 1st edn. Edited by V. Masson-Delmotte, A. Zhai, S.L. Pirani, C. Connors, S. Péan, N. Berger, Y. Caud, L. Chen, M.I. Goldfarb, M. Gomis, K. Huang, E. Leitzell, J.B.R. Lonnoy, T.K. Matthews, T. Maycock, O. Waterfield, R. Yelekçi, and B. Zhou. Cambridge: Cambridge University Press. doi:10.1017/9781009157896.

IPCC (2022). *Climate Change 2022 – Impacts, Adaptation and Vulnerability: Working Group II Contribution to the Sixth Assessment Report of the Intergovernmental Panel on Climate Change*. 1st edn. Edited by H.-O. Pörtner, D.C. Roberts, M. Tignor, E.S. Poloczanska, K. Mintenbeck, A. Alegría, M. Craig, S. Langsdorf, S. Löschke, V. Möller, A. Okem, and B. Rama. Cambridge: Cambridge University Press. doi:10.1017/9781009325844.

Itkonen, A. and Salonen, V.-P. (1994). The response of sedimentation in three varved lacustrine sequences to air temperature, precipitation and human impact. *Journal of Paleolimnology* 11(3), pp. 323–332. doi:10.1007/BF00677992.

Jane, S.F., Mincer, J.L., Lau, M.P., Lewis, A.S.L., Stetler, J.T. and Rose, K.C. (2023). Longer duration of seasonal stratification contributes to widespread increases in lake hypoxia and anoxia. *Global Change Biology* 29(4), pp. 1009–1023. doi:10.1111/gcb.16525.

Jansen, J., Simpson, G.L., Weyhenmeyer, G.A., Härkönen, L.H., Paterson, A.M., del Giorgio, P.A. and Prairie, Y.T. (2024). Climate-driven deoxygenation of northern lakes. *Nature Climate Change* 14(8), pp. 832–838. doi:10.1038/s41558-024-02058-3.

Johansson, M., Saarni, S. and Sorvari, J. (2019). Ultra-High-Resolution Monitoring of the Catchment Response to Changing Weather Conditions Using Online Sediment Trapping. *Quaternary* 2(2), p. 18. doi:10.3390/quat2020018.

Kaiserli, A., Voutsa, D. and Samara, C. (2002). Phosphorus fractionation in lake sediments – Lakes Volvi and Koronia, N. Greece. *Chemosphere* 46(8), pp. 1147–1155. doi:10.1016/S0045-6535(01)00242-9.

Li, H., Väliranta, M., Mäki, M., Kohl, L., Sannel, A.B.K., Pumpanen, J., Koskinen, M., Bäck, J. and Bianchi, F. (2020). Overlooked organic vapor emissions from thawing Arctic permafrost. *Environmental Research Letters* 15(10), p. 104097. doi:10.1088/1748-9326/abb62d.

Li, X., Peng, S., Xi, Y., Woolway, R.I. and Liu, G. (2022). Earlier ice loss accelerates lake warming in the Northern Hemisphere. *Nature Communications* 13(1), p. 5156. doi:10.1038/s41467-022-32830-y.

Lincoln, P., Tjallingii, R., Kosonen, E., Ojala, A., Abrook, A.M. and Martin-Puertas, C. (2025). Disruption of boreal lake circulation in response to mid-Holocene warmth; evidence from the varved sediments of Lake Nautajärvi, southern Finland. *Science of The Total Environment* 964, p. 178519. doi:10.1016/j.scitotenv.2025.178519.

MacIntyre, S. and Hamilton, D.P. (2024). Chapter 7 - Fate of Heat, in Jones, I.D. and Smol, J.P. (eds) *Wetzel's Limnology (Fourth Edition)*. San Diego: Academic Press, pp. 95–153. doi:10.1016/B978-0-12-822701-5.00007-0.

Magee, M.R. and Wu, C.H. (2017). Response of water temperatures and stratification to changing climate in three lakes with different morphometry. *Hydrology and Earth System Sciences* 21, pp. 6253–6274. doi:10.5194/hess-21-6253-2017.

Makri, S., Wienhues, G., Bigalke, M., Gilli, A., Rey, F., Tinner, W., Vogel, H. and Grosjean, M. (2021). Variations of sedimentary Fe and Mn fractions under changing lake mixing regimes, oxygenation and land surface processes during Late-glacial and Holocene times. *Science of The Total Environment* 755, p. 143418. doi:10.1016/j.scitotenv.2020.143418.

Mammarella, I., Gavrylenko, G., Zdorovennova, G., Ojala, A., K.-M, E., Zdorovennov, R., Stepanyuk, O., Palshin, N., Terzhevik, A., Vesala, T. and Heiskanen, J. (2018). Effects of similar weather patterns on the thermal stratification, mixing regimes and hypolimnetic oxygen depletion in two boreal lakes with different water transparency. *Boreal environment research* 23 (1–6), pp. 237–247. doi:10.60910/7r49-5wxy

Mann, M.E., Zhang, Z., Rutherford, S., Bradley, R.S., Hughes, M.K., Shindell, D., Ammann, C., Faluvegi, G. and Ni, F. (2009). Global Signatures and Dynamical Origins of the Little Ice Age and Medieval Climate Anomaly. *Science* 326(5957), pp. 1256–1260. doi:10.1126/science.1177303.

Mattsson, T., Kortelainen, P. and Räike, A. (2005). Export of DOM from Boreal Catchments: Impacts of Land Use Cover and Climate. *Biogeochemistry* 76(2), pp. 373–394. doi:10.1007/s10533-005-6897-x.

Mentzer, S.M. (2017). Micro XRF, in Nicosia, C. and Stoops, G. (eds) *Archaeological Soil and Sediment Micromorphology*. John Wiley & Sons, Ltd, pp. 431–440. doi:10.1002/9781118941065.ch41.

Messager, M.L., Lehner, B., Grill, G., Nedeva, I. and Schmitt, O. (2016). Estimating the volume and age of water stored in global lakes using a geo-statistical approach. *Nature Communications* 7(1), p. 13603. doi:10.1038/ncomms13603.

Metsähallitus (2017). Kevon luonnonpuiston ja Natura 2000 -alueen hoito- ja käyttösuunnitelma, *Metsähallituksen luonnonsuojelujulkaisuja*, C 145, p. 178.

Meyer-Jacob, C., Bindler, R., Bigler, C., Leng, M.J., Lowick, S.E. and Vogel, H. (2017). Regional Holocene climate and landscape changes recorded in the large subarctic lake Torneträsk, N Fennoscandia. *Palaeogeography, Palaeoclimatology, Palaeoecology* 487, pp. 1–14. doi:10.1016/j.palaeo.2017.08.001.

MML (2026). *Topographic database and Topographic map 1:100 000 (vector)*. National Land Survey of Finland. <https://www.maanmittauslaitos.fi/en/maps-and-spatial-data/datasets-and-interfaces/product-descriptions/topographic-database> (Accessed: 7 June 2026).

Noori, R., Woolway, R.I., Saari, M., Pulkkanen, M. and Kløve, B. (2022). Six Decades of Thermal Change in a Pristine Lake Situated North of the Arctic Circle. *Water Resources Research*, 58(9) p. e2021WR031543. doi:10.1029/2021WR031543.

Ojala, A.E.K. and Alenius, T. (2005). 10 000 years of interannual sedimentation recorded in the Lake Nautajärvi (Finland) clastic–organic varves. *Palaeogeography, Palaeoclimatology, Palaeoecology* 219(3), pp. 285–302. doi:10.1016/j.palaeo.2005.01.002.

Ojala, A.E.K., Kosonen, E., Weckström, J., Korkonen, S. and Korhola, A. (2013). Seasonal formation of clastic-biogenic varves: the potential for palaeoenvironmental interpretations. *GFF* 135(3–4), pp. 237–247. doi:10.1080/11035897.2013.801925.

O'Reilly, C.M., Sharma, S., Gray, D.K., Hampton, S.E., Read, J.S., Rowley, R.J., Schneider, P., Lenters, J.D., McIntyre, P.B., Kraemer, B.M., Weyhenmeyer, G.A., Straile, D., Dong, B., Adrian, R., Allan, M.G., Anneville, O., Arvola, L., Austin, J., Bailey, J.L., Baron, J.S., Brookes, J.D., de Eyto, E., Dokulil, M.T., Hamilton, D.P., Havens, K., Hetherington, A.L., Higgins, S.N., Hook, S., Izmest'eva, L.R., Joehnk, K.D., Kangur, K., Kasprzak, P., Kumagai, M., Kuusisto, E., Leshkevich, G., Livingstone, D.M., MacIntyre, S., May, L., Melack, J.M., Mueller-Navarra, D.C., Naumenko, M., Noges, P., Noges, T., North, R.P., Plisnier, P.-D., Rigosi, A., Rimmer, A., Rogora, M., Rudstam, L.G., Rusak, J.A., Salmaso, N., Samal, N.R., Schindler, D.E., Schladow, S.G., Schmid, M., Schmidt, S.R., Silow, E., Soylu, M.E., Teubner, K., Verburg, P., Voutilainen, A., Watkinson, A., Williamson, C.E. and Zhang, G. (2015). Rapid and highly variable warming of lake surface waters around the globe. *Geophysical Research Letters* 42(24), p. 10,773–10,781. doi:10.1002/2015GL066235.

Palmu, J.-P., Ojala, A., Virtasalo, J., Putkinen, N., Kohonen, J. and Sarala, P. (2021). Classification system of superficial (Quaternary) geological units in Finland. *Bulletin of the Geological Survey of Finland* 412, pp. 115–169. doi:10.30440/bt412.4.

Potts, P.J. and Webb, P.C. (1992). X-ray fluorescence spectrometry. *Journal of Geochemical Exploration* 44(1), pp. 251–296. doi:10.1016/0375-6742(92)90052-A.

Quante, L., Willner, S.N., Middelanis, R. and Levermann, A. (2021). Regions of intensification of extreme snowfall under future warming. *Scientific Reports* 11(1), p. 16621. doi:10.1038/s41598-021-95979-4.

Rantanen, M., Karpechko, A.Y., Lipponen, A., Nordling, K., Hyvärinen, O., Ruosteenoja, K., Vihma, T. and Laaksonen, A. (2022). The Arctic has warmed nearly four times faster than the globe since 1979. *Communications Earth & Environment* 3(1), p. 168. doi:10.1038/s43247-022-00498-3.

Renssen, H., Seppä, H., Crosta, X., Goosse, H. and Roche, D.M. (2012). Global characterization of the Holocene Thermal Maximum. *Quaternary Science Reviews* 48, pp. 7–19. doi:10.1016/j.quascirev.2012.05.022.

Renssen, H., Seppä, H., Heiri, O., Roche, D.M., Goosse, H. and Fichefet, T. (2009). The spatial and temporal complexity of the Holocene thermal maximum. *Nature Geoscience* 2(6), pp. 411–414. doi:10.1038/ngeo513.

Rothwell, R.G. and Croudace, I. w. (2015). Twenty Years of XRF Core Scanning Marine Sediments: What Do Geochemical Proxies Tell Us? In Croudace, I.W. and Rothwell, R.G. (eds) *Micro-XRF Studies of Sediment Cores: Applications of a non-destructive tool for the environmental sciences*. Dordrecht: Springer Netherlands, pp. 25–102. doi:10.1007/978-94-017-9849-5_2.

Saarni, S., Hartikainen, S., Meronen, S., Uurasjärvi, E., Kalliokoski, M. and Koistinen, A. (2021). Sediment trapping – An attempt to monitor temporal variation of microplastic flux rates in aquatic systems. *Environmental Pollution* 274, p. 116568. doi:10.1016/j.envpol.2021.116568.

Saarni, S., Lensu, A., Tammelin, M., Haltia, E. and Saarinen, T. (2017). Winter climate signal in boreal clastic-biogenic varves: a comprehensive analysis of three varved records from 1890 to 1990 AD with meteorological and hydrological data from Eastern Finland. *GFF* 139(4), pp. 314–326. doi:10.1080/11035897.2017.1389984.

Saarni, S., Soininen, T., Uurasjärvi, E., Hartikainen, S., Meronen, S., Saarinen, T. and Koistinen, A. (2023). Seasonal variation observed in microplastic deposition rates in boreal lake sediments. *Journal of Soils and Sediments* 23(4), pp. 1960–1970. doi:10.1007/s11368-023-03465-3.

Sander, M., Bengtsson, L., Holmquist, B., Wohlfarth, B. and Cato, I. (2002). The relationship between annual varve thickness and maximum annual discharge (1909–1971). *Journal of Hydrology* 263(1), pp. 23–35. doi:10.1016/S0022-1694(02)00030-6.

Santisteban, J.I., Mediavilla, R., López-pamo, E., Dabrio, C.J., Zapata, M.B., Ruiz, García, M.J., Gil, Castaño, S. and Martínez-alfaro, P.E. (2004). Loss on ignition: a qualitative or quantitative method for organic matter and carbonate mineral content in sediments? *Journal of Paleolimnology* 32(3), pp. 287–299. doi:10.1023/B:JOPL.0000042999.30131.5b.

Schmid, M., Hunziker, S. and Wüest, A. (2014). Lake surface temperatures in a changing climate: a global sensitivity analysis. *Climatic Change* 124(1), pp. 301–315. doi:10.1007/s10584-014-1087-2.

Sharma, S., Blagrave, K., Magnuson, J.J., O'Reilly, C.M., Oliver, S., Batt, R.D., Magee, M.R., Straile, D., Weyhenmeyer, G.A., Winslow, L. and Woolway, R.I. (2019). Widespread loss of lake ice around the Northern Hemisphere in a warming world. *Nature Climate Change* 9(3), pp. 227–231. doi:10.1038/s41558-018-0393-5.

Slaymaker, O., Souch, C., Menounos, B. and Filippelli, G. (2003). Advances in Holocene mountain geomorphology inspired by sediment budget methodology. *Geomorphology* 55(1), pp. 305–316. doi:10.1016/S0169-555X(03)00146-6.

Snowball, I., Sandgren, P. and Petterson, G. (1999). The mineral magnetic properties of an annually laminated Holocene lake-sediment sequence in northern Sweden. *The Holocene* 9(3), pp. 353–362. doi:10.1191/095968399670520633.

Soetaert, K., Hofmann, A.F., Middelburg, J.J., Meysman, F.J.R. and Greenwood, J. (2007). The effect of biogeochemical processes on pH. *Marine Chemistry* 105(1), pp. 30–51. doi:10.1016/j.marchem.2006.12.012.

Steinsberger, T., Schwefel, R., Wüest, A. and Müller, B. (2020). Hypolimnetic oxygen depletion rates in deep lakes: Effects of trophic state and organic matter accumulation. *Limnology and Oceanography* 65(12), pp. 3128–3138.

Syke (2014). *VALUE –selainpohjainen valuma-alueiden rajaustyökalu*. Finnish Environment Institute. <https://paikkatieto.ymparisto.fi/value/> (Accessed: 27 October 2024).

Syke (2024). *Hertta 5.7 environmental information system*, *Hydrological observations*. Finnish Environment Institute. <https://www.syke.fi/en/environmental-data/maps-and-information-services/open-environmental-information-systems> (Accessed: 3 November 2024).

Syke (2026). *Ranta10 - Shoreline 1:10 000 and river network (uomaverkosto)*. Finnish Environment Institute. <https://ckan.ymparisto.fi/dataset/%7BC40D8B4A-DC66-4822-AF27-7B382D89C8ED%7D> (Accessed: 5 June 2026).

Tiljander, M., Karhu, J.A. and Kauppila, T. (2006). Holocene records of carbon and hydrogen isotope ratios of organic matter in annually laminated sediments of Lake Korttajärvi, central Finland. *Journal of Paleolimnology* 36(3), pp. 233–243. doi:10.1007/s10933-006-9059-9.

Tiljander, M., Saarnisto, M., Ojala, A.E.K. and Saarinen, T. (2003). A 3000-year palaeoenvironmental record from annually laminated sediment of Lake Korttajarvi, central Finland. *Boreas* 32(4), pp. 566–577. doi:10.1111/j.1502-3885.2003.tb01236.x.

Tranvik, L.J., Downing, J.A., Cotner, J.B., Loiselle, S.A., Striegl, R.G., Ballatore, T.J., Dillon, P., Finlay, K., Fortino, K., Knoll, L.B., Kortelainen, P.L., Kutser, T., Larsen, S., Laurion, I., Leech, D.M., McCallister, S.L., McKnight, D.M., Melack, J.M., Overholt, E., Porter, J.A., Prairie, Y., Renwick, W.H., Roland, F., Sherman, B.S., Schindler, D.W., Sobek, S., Tremblay, A., Vanni, M.J., Verschoor, A.M., von Wachenfeldt, E. and Weyhenmeyer, G.A. (2009). Lakes and Reservoirs as Regulators of Carbon Cycling and Climate. *Limnology and Oceanography* 54(6), pp. 2298–2314.

Tylmann, W., Głowacka, P. and Szczerba, A. (2017). Tracking climate signals in varved lake sediments: research strategy and key sites for comprehensive process studies in the Masurian Lakeland. *Limnological Review* 17(3), pp. 159–166. doi:10.1515/limre-2017-0015.

Tylmann, W., Szpakowska, K., Ohlendorf, C., Woszczyk, M. and Zolitschka, B. (2012). Conditions for deposition of annually laminated sediments in small meromictic lakes: a case study of Lake Suminko (northern Poland). *Journal of Paleolimnology* 47(1), pp. 55–70. doi:10.1007/s10933-011-9548-3.

University of Turku (2026). *Tutkimus Kevon tutkimusasemalla*. <https://www.utu.fi/fi/yliopisto/matemaattis-luonnontieteellinen-tiedekunta/biodiversiteettiyksikko/kevo-tutkimus> (Accessed: 10 April 2026).

Vonk, J.E., Dickens, A.F., Giosan, L., Hussain, Z.A., Kim, B., Zipper, S.C., Holmes, R.M., Montlucon, D.B., Galy, V. and Eglinton, T.I. (2016). Arctic Deltaic Lake Sediments As Recorders of Fluvial Organic Matter Deposition. *Frontiers in Earth Science* 4. doi:10.3389/feart.2016.00077.

Wanner, H., Pfister, C. and Neukom, R. (2022). The variable European Little Ice Age. *Quaternary Science Reviews* 287, p. 107531. doi:10.1016/j.quascirev.2022.107531.

Weltje, G.J., Bloemsma, M.R., Tjallingii, R., Heslop, D., Röhl, U. and Croudace, I.W. (2015). Prediction of Geochemical Composition from XRF Core Scanner Data: A New Multivariate Approach Including Automatic Selection of Calibration Samples and Quantification of Uncertainties, in Croudace, I.W. and Rothwell, R.G. (eds) *Micro-XRF Studies of Sediment Cores: Applications of a non-destructive tool for the environmental sciences*. Dordrecht: Springer Netherlands (Developments in Paleoenvironmental Research), pp. 507–534. doi:10.1007/978-94-017-9849-5.

Weltje, G.J. and Tjallingii, R. (2008). Calibration of XRF core scanners for quantitative geochemical logging of sediment cores: Theory and application. *Earth and Planetary Science Letters* 274(3), pp. 423–438. doi:10.1016/j.epsl.2008.07.054.

Woolway, R.I. (2023). The pace of shifting seasons in lakes. *Nature Communications* 14(1), p. 2101. doi:10.1038/s41467-023-37810-4.

Woolway, R.I., Kraemer, B.M., Lenters, J.D., Merchant, C.J., O'Reilly, C.M. and Sharma, S. (2020). Global lake responses to climate change. *Nature Reviews Earth & Environment* 1(8), pp. 388–403. doi:10.1038/s43017-020-0067-5.

Woolway, R.I. and Merchant, C.J. (2019). Worldwide alteration of lake mixing regimes in response to climate change. *Nature Geoscience* 12(4), pp. 271–276. doi:10.1038/s41561-019-0322-x.

Woolway, R.I., Sharma, S., Weyhenmeyer, G.A., Debolskiy, A., Golub, M., Mercado-Bettín, D., Perroud, M., Stepanenko, V., Tan, Z., Grant, L., Ladwig, R., Mesman, J., Moore, T.N., Shatwell, T., Vanderkelen, I., Austin, J.A., DeGasperi, C.L., Dokulil, M., La Fuente, S., Mackay, E.B., Schladow, S.G., Watanabe, S., Marcé, R., Pierson, D.C., Thiery, W. and Jennings, E. (2021) Phenological shifts in lake stratification under climate change. *Nature Communications* 12(1), p. 2318. doi:10.1038/s41467-021-22657-4.

Xiao, Y. and Riise, G. (2021). Coupling between increased lake color and iron in boreal lakes. *Science of The Total Environment* 767, p. 145104. doi:10.1016/j.scitotenv.2021.145104.

Żarczyński, M., Wacnik, A. and Tylmann, W. (2019). Tracing lake mixing and oxygenation regime using the Fe/Mn ratio in varved sediments: 2000 year-long record of human-induced changes from Lake Żabińskie (NE Poland). *Science of The Total Environment* 657, pp. 585–596. doi:10.1016/j.scitotenv.2018.12.078.

Zillén, L., Snowball, I., Sandgren, P. and Stanton, T. (2003). Occurrence of varved lake sediment sequences in Varmland, west central Sweden: lake characteristics, varve chronology and AMS radiocarbon dating. *Boreas* 32(4), pp. 612–626. doi:10.1111/j.1502-3885.2003.tb01239.x.

Zolitschka, B., Francus, P., Ojala, A.E.K. and Schimmelmann, A. (2015). Varves in lake sediments – a review. *Quaternary Science Reviews* 117, pp. 1–41. doi:10.1016/j.quascirev.2015.03.019.

Appendices

Appendix 1. Basin and delta sampling periods

	Basin		**Delta**	
Sampling period	Set	Collected	Set	Collected
summer 2019	17.6.2019	26.9.2019	17.6.2019	26.9.2019
winter 2019–2020	26.9.2019	7.4.2020	26.9.2019	**
spring 2020**	7.4.2020	5.8.2020	**	5.8.2020
summer 2020*	5.8.2020	7.10.2020	5.8.2020	7.10.2020
winter 2020–2021	7.10.2020	2.4.2021	7.10.2020	3.4.2021
spring 2021	2.4.2021	18.6.2021	3.4.2021	18.6.2021
summer 2021	18.6.2021	28.9.2021	-	-
winter 2021–2022	28.9.2021	4.4.2022	28.9.2021	5.4.2022
spring 2022	4.4.2022	20.6.2022	5.4.2022	20.6.2022
summer 2022	29.6.2022	10.10.2022	29.6.2022	10.10.2022
winter 2022–2023	10.10.2022	25.3.2023	10.10.2022	25.3.2023
spring 2023	25.3.2023	19.6.2023	25.3.2023	19.6.2023
summer 2023	19.6.2023	11.10.2023	19.6.2023	11.10.2023

Sampling period shorter * or longer ** than intended

Appendix 2. Original sample IDs, sampling periods, dry masses, and subsample masses for LOI, u-XRF, and diatoms (not considered in this study)

ID	Sampling period	Study site	Dry mass (g)	Subsample LOI (g)	Subsample μ-XRF (g)	Supsample diatom (g)
1	summer 2019	delta	0.578	0.201	0.015	0.100
2	summer 2020*	delta	0.112	**0.075**	0.023	0.023
3	winter 2020–2021	delta	0.328	0.100	0.020	0.100
4	summer 2019	basin	0.852	0.201	0.041	0.100
5	summer 2020*	basin	0.414	0.200	0.037	0.100
6	winter 2019–2020	basin	0.295	0.101	0.035	0.100
7	summer 2021	basin	1.303	0.200	0.041	0.101
8	winter 2020–2021	basin	0.319	0.100	0.040	0.100
9	spring 2021	delta	3.523	0.500	0.028	0.100
10	spring 2021	basin	2.272	0.500	0.037	0.101
11	spring 2020**	basin	13.069	0.500	0.069	0.101
12	winter 2019–2020**	delta	22.141	0.500	0.057	0.101
13	summer 2022	delta	0.617	0.200	0.026	0.100
14	winter 2021–2022	delta	0.063	**0.027**	0.024	0.024
15	winter 2021–2022	basin	0.249	0.100	0.036	0.100
16	summer 2023	basin	1.266	0.200	0.036	0.200
17	summer 2023	delta	0.874	0.201	0.029	0.100
18	spring 2023	basin	1.399	0.500	0.031	0.100
19	winter 2022–2023	delta	0.196	0.101	0.032	0.032
20	winter 2022–2023	basin	0.384	0.100	0.040	0.100
21	summer 2022	basin	0.907	0.201	0.039	0.100
22	winter 2022–2023	delta	5.717	0.500	0.031	0.100
23	spring 2022	delta	19.126	0.500	0.076	0.101
24	spring 2022	basin	5.955	0.500	0.037	0.101

* Shorter sampling period

** Prolonged sampling period

Note: **Bold** subsample sizes were smaller than intended.

Appendix 3. Study site basin: µ-XRF data

Total elemental intensities (cps)

Sampling period	Al	Ca	Fe	K	Mn	P	S	Si	Ti
summer 2019	2.08	58.26	8050.34	5.07	768.11	0.39	1.79	134.72	3.65
winter 2019–2020	1.95	91.22	7659.66	3.42	551.29	1.23	2.45	143.4	2.22
spring 2020*	11.76	106.07	3977.98	30.82	188.17	0.13	2.27	251.58	60.91
summer 2020**	3.69	117.5	5957.81	9.5	592.8	0.14	0.78	243.14	11.58
winter 2020–2021	2.03	91.17	7765.44	4.45	523.61	0.7	2.4	141.64	2.7
spring 2021	5.68	81.81	6267.33	15.53	271.76	0.38	3.14	196.16	18.7
summer 2021	2.21	49.99	8013.03	5.23	1209.77	0.78	2.46	115.21	3.2
winter 2021–2022	1.65	58.52	7549.06	3.69	509.12	2.09	3.6	139.17	7.43
spring 2022	7.69	85.27	5049.83	20.2	194.04	0.32	4.09	187.66	29.38
summer 2022	2.36	45.78	7981.37	6.1	427.49	0.67	3.13	122.64	4.41
winter 2022–2023	1.65	73.03	9064.82	2.48	473.14	1.4	3.36	85.5	1.18
spring 2023	5.74	85.14	5316.65	15.92	237.81	0.69	5.32	160.88	17.19
summer 2023	2.56	71.23	7051.91	7.89	484.81	0.32	3.7	151.5	6.4

Clr-transformed elemental intensities and the sum of clr values for each sample

Sampling period	Al_{clr}	Ca_{clr}	Fe_{clr}	K_{clr}	Mn_{clr}	P_{clr}	S_{clr}	Si_{clr}	Ti_{clr}	Sum
summer 2019	-2.37	0.97	5.89	-1.48	3.54	-4.04	-2.52	1.80	-1.80	0
winter 2019–2020	-2.50	1.34	5.77	-1.94	3.14	-2.96	-2.27	1.80	-2.37	0
spring 2020*	-1.15	1.05	4.68	-0.18	1.63	-5.65	-2.79	1.92	0.50	-6E-16
summer 2020**	-1.93	1.53	5.46	-0.99	3.15	-5.20	-3.49	2.26	-0.79	2E-15
winter 2020–2021	-2.45	1.36	5.80	-1.66	3.11	-3.51	-2.28	1.80	-2.16	0
spring 2021	-1.78	0.89	5.23	-0.77	2.09	-4.48	-2.37	1.77	-0.58	0
summer 2021	-2.43	0.69	5.77	-1.57	3.88	-3.47	-2.32	1.52	-2.06	0
winter 2021–2022	-2.83	0.74	5.60	-2.03	2.90	-2.60	-2.05	1.60	-1.33	0
spring 2022	-1.53	0.87	4.95	-0.57	1.69	-4.71	-2.17	1.66	-0.19	-1E-15
summer 2022	-2.32	0.65	5.81	-1.37	2.88	-3.57	-2.03	1.64	-1.69	0
winter 2022–2023	-2.51	1.28	6.10	-2.11	3.14	-2.68	-1.80	1.43	-2.85	0
spring 2023	-1.83	0.86	5.00	-0.81	1.89	-3.95	-1.91	1.50	-0.74	9E-16
summer 2023	-2.32	1.00	5.60	-1.20	2.92	-4.40	-1.95	1.76	-1.41	0

Natural logarithms of the elemental intensity ratios

Sampling period	ln(K/Al)	ln(Si/Al)	ln(Si/K)	ln(Si/Ti)	ln(Ti/Al)	ln(Mn/Fe)
summer 2019	0.89	4.17	3.28	3.61	0.56	-2.35
winter 2019–2020	0.56	4.30	3.74	4.17	0.13	-2.63
spring 2020*	0.96	3.06	2.10	1.42	1.64	-3.05
summer 2020**	0.95	4.19	3.24	3.04	1.14	-2.31
winter 2020–2021	0.78	4.25	3.46	3.96	0.29	-2.70
spring 2021	1.01	3.54	2.54	2.35	1.19	-3.14
summer 2021	0.86	3.95	3.09	3.58	0.37	-1.89
winter 2021–2022	0.80	4.43	3.63	2.93	1.50	-2.70
spring 2022	0.97	3.19	2.23	1.85	1.34	-3.26
summer 2022	0.95	3.95	3.00	3.33	0.63	-2.93
winter 2022–2023	0.41	3.95	3.54	4.28	-0.34	-2.95
spring 2023	1.02	3.33	2.31	2.24	1.10	-3.11
summer 2023	1.13	4.08	2.95	3.16	0.92	-2.68

Sampling period longer * or shorter ** than intended

Appendix 4. Study site delta: µ-XRF data

Total elemental intensities (cps)

Sampling period	Al	Ca	Fe	K	Mn	P	S	Si	Ti
summer 2019	2.65	78.18	4809.78	9.18	288.75	0.22	1.18	205.46	17.36
winter 2019–2020*	8.98	147.58	3130.23	23.99	101.44	0.71	9.78	175.19	28.58
summer 2020**	2.8	96.64	4796.66	8.85	366.65	0.27	5.29	219.17	12.19
winter 2020–2021	2.91	97.97	4873.03	11.54	226.01	0.22	3.38	210.04	14.57
spring 2021	7.55	101.79	4494.58	19.49	177.8	0.34	4.4	215.01	28.33
winter 2021–2022	2	89.22	4668.16	9.58	218.04	0.55	10.02	268.37	11.39
spring 2022	13.3	149.76	3271.7	28.63	104.08	0.22	4.42	246.45	36.12
summer 2022	2.54	64.79	5762.14	8.76	213.52	0.12	2.9	226.47	10.33
winter 2022–2023	1.56	77.83	7728.38	5.3	227.17	0.38	3.04	179.75	4.44
spring 2023	5.69	104.81	4546.86	16.81	177.78	0.21	4.67	220.99	23.34
summer 2023	4.04	78.82	4856.41	11.99	164.56	0.08	3.68	257.79	39.14

Clr-transformed elemental intensities and the sum of clr values for each sample

Sampling period	Al_{clr}	Ca_{clr}	Fe_{clr}	K_{clr}	Mn_{clr}	P_{clr}	S_{clr}	Si_{clr}	Ti_{clr}	Sum
summer 2019	-2.19	1.19	5.31	-0.95	2.50	-4.68	-3.00	2.16	-0.32	6E-16
winter 2019–2020*	-1.53	1.27	4.33	-0.54	0.90	-4.06	-1.44	1.44	-0.37	0
summer 2020**	-2.35	1.19	5.10	-1.20	2.53	-4.69	-1.71	2.01	-0.88	0
winter 2020–2021	-2.24	1.28	5.19	-0.86	2.12	-4.82	-2.09	2.04	-0.63	-9E-16
spring 2021	-1.57	1.03	4.82	-0.62	1.59	-4.67	-2.11	1.78	-0.25	-6E-16
winter 2021–2022	-2.75	1.05	5.00	-1.19	1.94	-4.04	-1.14	2.15	-1.01	0
spring 2022	-1.05	1.37	4.45	-0.29	1.01	-5.15	-2.15	1.87	-0.05	5E-16
summer 2022	-2.18	1.06	5.55	-0.94	2.25	-5.23	-2.05	2.31	-0.78	0
winter 2022–2023	-2.63	1.28	5.88	-1.41	2.35	-4.04	-1.96	2.12	-1.58	0
spring 2023	-1.74	1.17	4.94	-0.66	1.70	-5.04	-1.94	1.92	-0.33	0
summer 2023	-1.92	1.05	5.17	-0.83	1.79	-5.84	-2.01	2.24	0.35	8E-16

Natural logarithms of the elemental intensity ratios

Sampling period	ln(K/Al)	ln(Si/Al)	ln(Si/K)	ln(Si/Ti)	ln(Ti/Al)	ln(Mn/Fe)
summer 2019	1.24	4.35	3.11	2.47	1.88	-2.81
winter 2019–2020*	0.98	2.97	1.99	1.81	1.16	-3.43
summer 2020**	1.15	4.36	3.21	2.89	1.47	-2.57
winter 2020–2021	1.38	4.28	2.90	2.67	1.61	-3.07
spring 2021	0.95	3.35	2.40	2.03	1.32	-3.23
winter 2021–2022	1.57	4.90	3.33	3.16	1.74	-3.06
spring 2022	0.77	2.92	2.15	1.92	1.00	-3.45
summer 2022	1.24	4.49	3.25	3.09	1.40	-3.30
winter 2022–2023	1.22	4.75	3.52	3.70	1.05	-3.53
spring 2023	1.08	3.66	2.58	2.25	1.41	-3.24
summer 2023	1.09	4.16	3.07	1.89	2.27	-3.38

Sampling period longer * or shorter ** than intended

Appendix 5. Study site basin: PCA of clr-transformed elemental intensities by sampling period

Eigenvalues and explained variance

PC	Eigenvalue	Variance (%)
1	2.65	78.84
2	0.47	13.96
3	0.10	3.11
4	0.10	2.85
5	0.03	0.75
6	0.01	0.32
7	0.00	0.13
8	0.00	0.03
9	0.00	0.00

Scores

Sampling period	PC 1	PC 2	PC 3	PC 4	PC 5	PC 6	PC 7	PC 8	PC 9
summer 2019	0.67	-0.76	0.15	0.25	0.02	0.07	0.03	0.00	0.00
winter 2019–2020	1.63	-0.01	-0.27	-0.39	-0.08	-0.04	-0.08	-0.07	0.00
spring 2020*	-3.28	-0.04	-0.04	-0.10	-0.09	-0.02	0.07	-0.05	0.00
summer 2020**	-1.20	-1.59	0.04	-0.41	0.02	0.01	-0.01	0.04	0.00
winter 2020–2021	1.10	-0.24	-0.33	-0.15	0.07	-0.04	-0.06	0.02	0.00
spring 2021	-1.32	0.28	-0.01	0.01	-0.01	0.13	-0.04	0.02	0.00
summer 2021	1.29	-0.46	0.42	0.44	-0.30	-0.13	0.01	0.00	0.00
winter 2021–2022	1.26	0.79	0.74	-0.50	0.14	-0.01	0.04	0.00	0.00
spring 2022	-1.97	0.64	-0.09	0.08	-0.01	0.01	0.04	-0.01	0.00
summer 2022	0.61	0.25	0.12	0.32	0.01	0.23	-0.06	-0.01	0.00
winter 2022–2023	2.27	0.34	-0.54	-0.03	-0.06	0.04	0.14	0.03	0.00
spring 2023	-0.97	0.98	-0.09	0.04	-0.10	-0.12	-0.08	0.05	0.00
summer 2023	-0.07	-0.17	-0.08	0.44	0.40	-0.13	0.00	-0.02	0.00

Sampling period longer * or shorter ** than intended

Loadings

Element	PC 1	PC 2	PC 3	PC 4	PC 5	PC 6	PC 7	PC 8	PC 9
Al	-0.27	0.02	-0.31	0.09	-0.62	0.13	0.38	-0.40	0.33
Ca	0.01	-0.22	-0.55	-0.48	0.17	-0.40	0.15	0.31	0.33
Fe	0.24	-0.17	-0.07	0.15	0.26	0.74	0.27	0.28	0.33
K	-0.36	0.00	-0.09	0.35	-0.23	0.01	-0.60	0.47	0.33
Mn	0.35	-0.57	0.41	0.29	-0.16	-0.38	0.10	-0.04	0.33
P	0.53	0.50	0.21	-0.39	-0.36	0.05	-0.17	0.09	0.33
S	0.12	0.51	-0.17	0.50	0.43	-0.30	0.10	-0.20	0.33
Si	-0.06	-0.23	-0.02	-0.26	0.29	0.19	-0.51	-0.61	0.33
Ti	-0.56	0.16	0.59	-0.25	0.20	-0.04	0.29	0.11	0.33

Appendix 6. Study site delta: PCA of clr-transformed elemental intensities by sampling period

Eigenvalues and explained variance

PC	Eigenvalue	Variance (%)
1	0.99	62.76
2	0.31	19.40
3	0.17	10.71
4	0.06	3.98
5	0.03	1.78
6	0.01	0.72
7	0.01	0.45
8	0.00	0.21
9	0.00	0.00

Scores

Sampling period	PC1	PC 2	PC 3	PC 4	PC 5	PC 6	PC 7	PC 8	PC 9
summer 2019	0.12	0.91	0.63	-0.35	-0.08	-0.05	-0.03	-0.03	0.00
summer 2020*	0.69	-0.02	-0.20	-0.16	0.40	0.03	0.07	-0.05	0.00
winter 2020–2021	0.17	0.12	0.03	-0.02	0.06	-0.12	0.01	0.13	0.00
spring 2021	-0.68	-0.38	0.34	-0.11	-0.04	0.24	-0.04	0.02	0.00
winter 2021–2022	1.06	-0.90	-0.36	-0.30	-0.17	-0.07	-0.06	-0.02	0.00
spring 2022	-1.65	-0.59	0.33	0.20	0.03	-0.14	0.02	-0.06	0.00
summer 2022	0.25	0.49	-0.30	0.35	0.06	0.01	-0.18	-0.02	0.00
winter 2022–2023	1.64	-0.03	0.31	0.39	-0.14	0.04	0.11	-0.01	0.00
spring 2023	-0.59	-0.19	-0.04	0.06	0.06	0.05	0.00	0.07	0.00
summer 2023	-1.01	0.58	-0.74	-0.05	-0.18	0.03	0.10	-0.02	0.00

Sampling period shorter* than intended
Note: Winter 2019–2020 was excluded from PCA calculations.

Loadings

Element	PC 1	PC 2	PC 3	PC 4	PC 5	PC 6	PC 7	PC 8	PC 9
Al	-0.48	-0.11	0.30	0.36	0.31	0.37	0.04	-0.44	0.33
Ca	-0.01	-0.02	0.15	0.16	0.18	-0.65	0.61	0.14	0.33
Fe	0.29	0.38	-0.05	0.53	-0.43	0.35	0.15	0.24	0.33
K	-0.31	-0.09	0.15	0.08	0.05	-0.17	-0.58	0.62	0.33
Mn	0.37	0.47	-0.02	-0.32	0.63	0.15	-0.10	0.01	0.33
P	0.42	-0.44	0.56	-0.34	-0.27	0.13	-0.01	-0.07	0.33
S	0.15	-0.58	-0.69	0.04	0.15	0.14	0.06	0.05	0.33
Si	0.07	0.17	-0.20	0.06	-0.28	-0.46	-0.43	-0.58	0.33
Ti	-0.50	0.22	-0.19	-0.58	-0.34	0.15	0.27	0.05	0.33

Appendix 7. Observed durations of stratified water column, ice cover, and snow cover

Stratification periods					
Thermal stratification			Inverse stratification		
Onset	Offset	Duration (days)	Onset	Offset	Duration (days)
no data	20.9.2019	no data	17.10.2019	26.5.2020	222
*	*	*	21.10.2020	20.5.2021	211
4.6.2021	11.9.2021	99	31.10.2021	15.5.2022	196
31.5.2022	13.9.2022	105	22.10.2022	14.5.2023	204
10.6.2023	7.9.2023	89	10.10.2023		

* Stable thermal stratification was not observed in summer 2020.

Ice coverage (Syke, 2024)

Ice on	Ice off	Ice cover (days)
22.10.2019	3.6.2020	225
21.11.2020	29.5.2021	189 (210*)
20.10.2021	25.5.2022	217
12.11.2022	21.5.2023	190

* Period of complete ice coverage was observed prior to the stable ice cover (31.10.2020).

Snow cover duration and maximum snow depths (FMI, 2024a)

Onset (> 2 cm)	Offset (< 2 cm)	Snow cover (days)	Max. depth (cm)
29.9.2019	30.9.2019		
16.10.2019	**26.5.2020**	**223**	107
17.10.2020	16.11.2020		
20.11.2020			
22.11.2020	29.11.2020		
1.12.2020	**16.5.2021**	**166**	54
16.10.2021			
21.10.2021			
23.10.2021	2.11.2021		
6.11.2021	**15.5.2022**	**190**	78
22.10.2022	23.10.2022		
27.10.2022	5.11.2022		
11.11.2022	**13.5.2023**	**183**	89
5.10.2023			
8.10.2023			

Note: Persistent snow cover period **in bold**